ELSEVIER

Journal of Magnetism and Magnetic Materials 163 (1996) 39–69

Journal of magnetism and magnetic materials

Theory of magnetostatic waves for in-plane magnetized anisotropic films

M.J. Hurben, C.E. Patton *

Department of Physics, Colorado State University, Fort Collins, CO 80523, USA

Received 31 July 1995; revised 7 March 1996

Abstract

A modified formulation of the Damon–Eshbach theory of magnetostatic waves for in-plane magnetized anisotropic films is presented. New results, relative to the usual backward volume wave, nonreciprocal surface wave, and surface mode critical angle properties for isotropic films, are obtained for films with various anisotropies. These include: (i) Surface mode suppression. (ii) A second critical propagation angle for which the backward volume band of dispersion branches becomes inverted and the dispersion curves change to a forward volume mode character. (iii) Mode conversion and a reentrant mode character for the lowest order dispersion branch; a volume mode character at low wave number which converts to a surface character at high wave number. At the conversion point, this mode corresponds to a propagating plane wave with a uniform mode profile across the film thickness but at nonzero propagation wave number. (iv) A third critical in-plane propagation angle at which the surface mode dispersion branch vanishes and the lowest order branch reverts to a pure volume mode character.

Keywords: Magnetostatic waves; Magnetic excitations; Magnetic thin films

1. Introduction

As discussed in an earlier paper on the theory of magnetostatic waves for in-plane magnetized isotropic films [1], magnetic excitations in solids at microwave frequencies have been a subject of continuing study since the pioneering theory of spin waves by Holstein and Primakoff [2], the discovery of ferromagnetic resonance (FMR) by Griffiths [3], and Kittel's linear response theory for FMR [4]. A special class of magnetic excitations which includes long wavelength propagating modes as well as the usual uniform mode FMR, with the generic name 'magnetostatic modes', has been important for fundamental reasons and for device applications. These excitations are termed 'magnetostatic' because for a mode at a given wave number, the mode frequency is *much less* than the corresponding electromagnetic frequency. The label 'magnetostatic modes' is often taken to mean the wavelengths are also sufficiently long that exchange may be neglected. The neglect of exchange, however, has nothing to do with the 'magnetostatic approximation', since the approximation places no lower limit on

* Corresponding author. Fax: + 1-970-491-7947.

0304-8853/96/$15.00 Copyright © 1996 Elsevier Science B.V. All rights reserved.
PII S0304-8853(96)00294-6

wavelength. In experiments on real materials, the wavelengths of the excited modes are generally on the order of the size of the sample under study. These excitations have wavelengths which are sufficiently small to satisfy the magnetostatic approximation and sufficiently large, under many circumstances, to neglect exchange.

Numerous papers on the theory of magnetostatic modes have made significant contributions to the understanding of magnetic excitations in solids. The theory was first reported for spheres by Walker [5]. Here, one obtains various sequences of standing modes which are often termed 'Walker modes'. The mode patterns are much like the normal vibration modes for elastic waves. Röschmann and Dötsch [6] have compiled a practical review of Walker mode theory for spheres.

The theory of magnetostatic mode excitations for ferromagnetic slabs and thin films was first developed by Damon and Eshbach [7]. The theory was for flat, unbounded films or slabs and yielded various propagating modes with wave vectors in the film or slab plane. These propagating modes are often termed magnetostatic waves (MSW). The terms 'magnetostatic modes', 'Walker modes', and 'magnetostatic waves' are often used interchangeably in the literature. The theory of Damon and Eshbach (DE) has served as the basis for numerous experimental studies of magnetic excitations in thin films and slabs of ferrite materials as well as for many microwave signal processing device applications. Two symposia and two recent textbooks provide a good review of the device physics and applications for thin slab and film MSW theory [8–10].

The theory of Damon and Eshbach yields two types of propagating waves: (a) backward volume waves (BVW) for reciprocal in-plane propagation at any angle relative to the field and magnetization direction and (b) a nonreciprocal surface wave for in-plane propagation at angles greater than some critical angle ϕ_c relative to the field and magnetization direction. The term 'reciprocal' denotes modes for which propagation is possible along both $+\boldsymbol{k}$ and $-\boldsymbol{k}$ directions, where $\boldsymbol{k}$ denotes a specific in-plane wave vector. 'Nonreciprocal' denotes modes associated with one surface in the high $|\boldsymbol{k}|$ limit and for which propagation is possible only for either $+\boldsymbol{k}$ or $-\boldsymbol{k}$, but not both. Ref. [1] provides an extensive review of the original DE theory, along with additional insight into the physical properties of the backward volume modes and the surface mode from the theory.

The original DE theory was for isotropic ferromagnetic materials. Interest in magnetic devices for frequencies in the millimeter wave regime has stimulated a re-examination of high anisotropy ferrites [11,12]. Such materials are desirable for millimeter wave applications because of their large anisotropy fields, up to 20 kOe or more. The proper utilization of such materials can yield FMR peaks at frequencies in excess of 50 GHz for relatively modest magnetic fields. These materials offer unique possibilities for conventional bulk ferrite as well as thin film type millimeter wave devices [13]. In addition to these high frequency applications, advances in preparation techniques for magnetic films, magnetic film sandwiches, and magnetic multilayers have resulted in new magnetic properties heretofore unrealized [14]. In many cases, such films have unique anisotropies which can significantly affect the nature of the magnetostatic waves in these structures. Heinrich and Cochran [15] provide a review of the magnetic properties of such metallic films and multilayers.

This paper is a sequel to Ref. [1]. The purpose of this work was to examine the effect of magnetic anisotropy on the properties of magnetostatic waves for in-plane magnetized thin slabs and films. This paper presents modifications of the DE theory for anisotropic films and examines the effect of these changes on magnetostatic wave properties for several basic categories of anisotropic materials. Anisotropy is found to have significant effects on both volume and surface modes. Sufficient anisotropy in materials similar to yttrium iron garnet can actually suppress the DE surface mode and produce a volume mode only situation. In materials such as iron or hexagonal ferrite, the DE volume and surface mode properties are modified in a different way. Depending on the specific parameters, one finds one or two new critical angles, one for BVW band inversion to create a forward volume wave (FVW) band of excitations for in-plane magnetized slabs, and one for a merging of the surface mode band edge back into the volume mode band. The band inversion effect, in combination with the co-existence of a surface mode and FVW modes at the same propagation angle, results in a re-entrant MSW dispersion branch for which a uniform mode profile across the film can occur at two distinct frequencies. The lowest frequency corresponds to FMR. The higher frequency corresponds to a propagating mode with a uniform dynamic response profile across the film.

A third paper will consider out-of-plane magnetized films. This geometry leads to effects which are closely related to the anisotropic effects presented below. A magnetic thin film or slab, after all, is inherently anisotropic due to shape. Out-of-plane static fields lead to new dispersion and mode properties.

Various authors have considered the influence of anisotropy on ferromagnetic resonance [4,16–20], general spin wave properties [21,22], spin wave instability processes [21–31], and magnetostatic modes [32–39]. Some aspects of the additional critical angle, re-entrant surface mode, and band inversion effects for single layer films are contained in Refs. [32,35,38,39]. Many of these effects have also been predicted for multilayer structures [40–42].

As with Ref. [1], this work does not consider the effects of exchange or the explicit boundary conditions on the dynamic magnetization response at the film surfaces which must be included when exchange is considered. The upper limit on wave number for which exchange may be neglected in the spin wave dispersion for typical ferrite materials is approximately 10^4 rad/cm. For typical films in the 1–10 μm thickness range, the corresponding wave number thickness product is 1–10, the same as the scale limits for the effects to be considered below.

Exchange, however, represents more than a simple term in the energy which can be neglected in certain limits. The inclusion of exchange complicates the theoretical problem greatly. Exchange does lead to important modifications in the theory, such as a lifting of the degeneracy of various MSW dispersion branches in various low- and high-wavenumber limits, as well as branch crossover and repulsion. Exchange also brings into play the explicit effect of surface boundary conditions on the dynamic components of the magnetization vector, through pinning effects. Pinning plays no explicit role in the DE theory. However, as made evident in Ref. [1], quasi-pinning effects do occur at large wave numbers.

References on exchange effects include Sparks [43], DeWames and Wolfram [44], Wolfram and DeWames [45], Kalinikos [46], and Kalinikos and Slavin [47]. References on pinning include Kittel [48] and Rado and Weertman [49]. The general problem of magnetic excitations in thin films and multilayers, as well as the effects of exchange and surface anisotropy on such excitations, has been addressed by Patton [50], Hillebrands [51], Stamps and Hillebrands [52], and Cottam [53].

2. Damon–Eshbach formalism for anisotropic films

This section describes the extension of the Damon–Eshbach theory for the propagating magnetostatic modes of an isotropic thin film or slab of infinite extent to the case of films or slabs with anisotropy. The formal development follows the same notation and sequence of equations given in Ref. [1]. The development is in terms of two effective magnetic field parameters, H_α and H_β, which play roles similar to the role of the single magnetic field parameter H_0 in the DE theory. These two field parameters contain terms related to anisotropy and give rise to new effects.

2.1. The in-plane magnetized anisotropic film geometry

As in Ref. [1], consider a flat unbounded ferromagnetic film which is magnetized by the application of an external magnetic field in the plane of the film. Now, however, the film is assumed to be magnetically anisotropic. Fig. 1 shows a film placed in a right-handed $\boldsymbol{X}$–$\boldsymbol{Y}$–$\boldsymbol{Z}$ coordinate system so that the plane of the film coincides with the X–Y plane. The static external field $\boldsymbol{H}_0$ is in-plane at an angle Θ relative to the X-axis and the saturation magnetization vector $\boldsymbol{M}_s$ is in-plane and at some angle Φ relative to the X-axis. The film is infinite in the X- and Y-directions and has a thickness S in the Z-direction. The rectangular box is for illustrative purposes only and is not intended to indicate a bounded rectangular film or slab. Explicit connections between the $\boldsymbol{X}$–$\boldsymbol{Y}$–$\boldsymbol{Z}$ reference frame and anisotropy will be given shortly. An additional set of orthogonal axes, denoted by $\boldsymbol{x}$, $\boldsymbol{y}$, and z, is also shown. The x-axis is along the $\boldsymbol{M}_s$ vector and the z-axis is co-linear with the

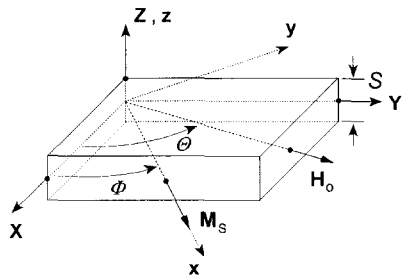

Fig. 1. Film, field, and magnetization geometry for an in-plane magnetized anisotropic film of thickness S. The right handed $X-Y-Z$ coordinate system is tied to the magnetic anisotropy of the sample. The static magnetic field $\boldsymbol{H}_0$ and the static saturation magnetization vector $\boldsymbol{M}_S$ are in-plane and aligned at angles Θ and Φ to the X-axis, respectively. The $x-y-z$ coordinate system is tied to the direction of $\boldsymbol{M}_S$ and the film normal, as indicated.

Z-axis. This reference frame will be termed the precession or 'P' frame, because the dynamic response will involve the precession of the total magnetization vector $\boldsymbol{M}$ about the x-direction. This P frame will be important for the dynamic response analysis.

Anisotropy is introduced into the problem by considering the magnetization vector to 'prefer' certain directions over others according to some directional dependent free energy density. Rather than develop an abstract theory for the general case, the focus here will be on real effects in real films of real magnetic materials of current technological interest, such as yttrium iron garnet (YIG), epitaxial iron, and hexagonal ferrite. From this perspective, it is important, even at this early stage, to introduce specific anisotropy cases upon which to develop the theory. For YIG or iron films, the X-, Y-, and Z-axes will represent the crystallographic [100] directions for the cubic single crystal. For hexagonal ferrite, the X-axis will represent the easy axis for a material with uniaxial anisotropy. An appropriate magnetocrystalline anisotropy free energy density which contains these situations may be written, to lowest order, as

$$F_A = K_U\left(1 - M_X^2/M_S^2\right) + K_1\left(M_X^2M_Y^2 + M_Y^2M_Z^2 + M_Z^2M_X^2\right)/M_S^4. \tag{1}$$

In Eq. (1), K_U denotes a uniaxial anisotropy energy density parameter, K_1 denotes a first order cubic anisotropy energy density parameter, and the $M_{X,Y,Z}$ denote the X-, Y-, and Z-components of the magnetization vector in the X–Y–Z sample reference frame.

Typical values of K_1 are in the -6×10^3 erg/cm^3 range for YIG [54] and in the $+5\times10^5$ erg/cm^3 range for single crystal iron [55]. Typical values of K_U for hexagonal barium ferrite are in the $+3\times10^6$ erg/cm^3 range [54]. Typical values of the saturation induction $4\pi M_S$ for these same three materials are 1750 [54], 21 000 [55], and 4700 G [56], respectively. These material parameters correspond to a cubic anisotropy field $H_A = 2K_1/M_S$ of about -86 and $+600$ Oe for YIG and iron, respectively, and a uniaxial anisotropy field $H_U = 2K_U/M_S$ for barium ferrite in the 16 000 Oe range. Explicit considerations for these three special cases will be a part of the analysis and results in subsequent sections. These cases will be cited as 'YIG', 'IRON', and 'HEX'. For reference purposes, the values of the saturation induction $4\pi M_S$, the anisotropy field H_A or H_U, two effective stiffness fields H_α and H_β for special values of H_0, Θ, and Φ, and the applicable critical propagation angles ϕ_c, ϕ_x, and ϕ_p, are given in Table 1. The concept of effective stiffness fields and the above critical angles will be considered shortly. The special cases in Table 1 are for situations with the field and magnetization collinear and along principal directions, e.g. for conditions in which $\Theta = \Phi$ is satisfied.

Fig. 1 shows only the situation at static equilibrium. It is convenient to deal with the dynamic response in terms of the x–y–z precession frame in Fig. 1, for which the x-axis is aligned with $\boldsymbol{M}_S$, the y-axis is in-plane and orthogonal to the x-axis, and the third orthogonal z-axis is perpendicular to the film and coincident with the crystallographic Z-axis. In this frame, the lowest order terms in a small amplitude dynamic response will involve only the y- and z- components of the total magnetization vector $\boldsymbol{M}$.

Table 1
Summary of material parameters, stiffness fields, and critical angles for 'YIG', 'IRON', and 'HEX' materials

	YIG	IRON	HEX
Saturation induction, $4\pi M_s$	1750 G	21 000 G	4700 G
Anisotropy character	Cubic	Cubic	Uniaxial
	[111] easy axes	[100] easy axes	easy c-axis
Anisotropy field	$H_A \approx -86$ Oe	$H_A \approx +600$ Oe	$H_U \approx 16000$ Oe
Out-of-plane stiffness field, H_α	957 Oe [a]	1300 Oe [b]	20 kOe [c]
In-plane stiffness field, H_β	1086 Oe [a]	400 Oe [b]	4 kOe [c]
Critical angles	$\phi_c = 39.3°$ [a]	$\phi_c = 7.7°$ [b]	$\phi_c = 23.7°$ [c]
		$\phi_x = 36.7°$ [b]	$\phi_x = 26.6°$ [c]
			$\phi_p = 30.8°$ [c]

[a] $H_0 = 1$ kOe, $\Theta = \Phi = 45°$.
[b] $H_0 = 1$ kOe, $\Theta = \Phi = 45°$.
[c] $H_0 = 20$ kOe, $\Theta = \Phi = 90°$.

Fig. 2 shows the same film sample as in Fig. 1, but now in a precession frame context with $\boldsymbol{M}_s$ along the positive x-direction. As in Ref. [1], the objective of the problem is to determine the dynamic propagating normal modes for the film. The wave vector $\boldsymbol{k}$ shown in Fig. 2 is for a general in-plane propagation direction. The in-plane propagation angle relative to the x-axis is designated by ϕ. Dashed lines show the basic x–y plane film geometry. Keep in mind that the anisotropic character of the film is referenced to the X–Y–Z sample frame through Eq. (1).

The magnetization response vector $\boldsymbol{M}(\boldsymbol{r},t)$ is shown schematically in the Fig. 2 insert. In this classical treatment, one requires that $|\boldsymbol{M}|$ be constant and equal to the saturation magnetization M_s. The $\boldsymbol{M}$-vector may then be conveniently separated into two parts, a static component in the x-direction which is equal to M_s and a dynamic magnetization response vector $\boldsymbol{m}(\boldsymbol{r},t)$. In the small signal limit in which $|\boldsymbol{m}(\boldsymbol{r},t)| \ll M_s$ is satisfied, to lowest order $\boldsymbol{m}$ has only transverse components m_y and m_z. This transverse response is indicated schematically by the precession circle in the insert. The arrow on the circle designates the Larmor precessional nature of the expected response. Fig. 2 is identical to Fig. 1 in Ref. [1], except for the absence of the in-plane field $\boldsymbol{H}_0$ in the x-direction. In the anisotropic situation considered here, $\boldsymbol{H}_0$ is in-plane but at some angle $(\Theta - \Phi)$ relative to the x-axis.

The normal modes will consist of specific plane waves of the form

$$m_{y,z} = m_{yo,zo}(z)\exp\{i[\boldsymbol{k}\cdot\boldsymbol{r} - \omega(k)t]\}, \tag{2}$$

with $m_{yo,zo}(z)$ profile functions which depend on one or more branch indices, as well as the various k, ϕ, S,

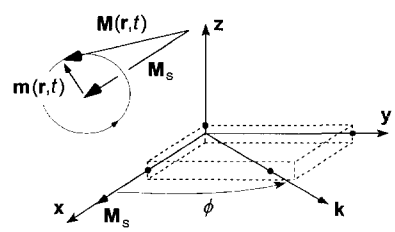

Fig. 2. Film, field, and magnetization shown in the $x-y-z$ precession frame geometry. The vectors $\boldsymbol{M}_s$ and $\boldsymbol{k}$ designate the saturation magnetization and the in-plane wave vector for a general propagating normal mode, respectively. The propagation angle relative to the x-axis is given by ϕ. The total magnetization response vector $\boldsymbol{M}(\boldsymbol{r},t)$ is shown in the insert, with the precessing $\boldsymbol{M}$-vector separated into two parts, a static component in the x-direction which is equal to M_s and a dynamic magnetization response vector $\boldsymbol{m}(\boldsymbol{r},t)$. The arrow on the precession circle designates the sense of the expected response.

M_s, H_0, Θ, K_U, and K_1 parameters. Note that the orientation angle Φ for the static magnetization $\boldsymbol{M}_s$ vector will be determined from the requirement of static equilibrium and specifically obtained in terms of H_0, Θ, K_U and K_1. The $\omega(k)$ dispersion curves for the normal modes will also depend on these same parameters. For in-plane propagation, the $\boldsymbol{r}$-vector in Eq. (2) is specifically in-plane.

2.2. Equation of motion and magnetic response

As for the isotropic case considered in Refs. [1,7], the starting point for the analysis is the equation of motion for the magnetization $\boldsymbol{M}$

$$\frac{d\boldsymbol{M}}{dt} = -\gamma(\boldsymbol{M}\times\boldsymbol{H}). \tag{3}$$

In Eq. (3), γ denotes the gyromagnetic ratio for the electron magnetic moments which make up the material and is taken as positive. For free electron moments with a Landé g-factor, $g = 2$, one has $\gamma = 1.76\times 10^7$ rad/Oe s in Gaussian units and $\gamma = 2.8$ GHz/kOe in practical units. In the $\boldsymbol{x}$–$\boldsymbol{y}$–$\boldsymbol{z}$ precession frame and to lowest order in transverse components, $\boldsymbol{M}$ is simply given by $\boldsymbol{M} = M_s\boldsymbol{e}_x + m_y\boldsymbol{e}_y + m_z\boldsymbol{e}_z$, where $\boldsymbol{e}_x$, $\boldsymbol{e}_y$, and $\boldsymbol{e}_z$ denote unit vectors in the x-, y-, and z-directions, respectively, and the $m_{y,z}$ have the plane wave form defined in Eq. (2). In the above formulae and for all analyses which follow, the Gaussian system of units is used.

The total magnetic field $\boldsymbol{H}$ consists of the x-directed static effective field $\boldsymbol{H}_S$ to be defined shortly, additional dynamic effective field components related to the $m_{y,z}$ through anisotropy considerations, and a dynamic Maxwellian field $\boldsymbol{h}(\boldsymbol{r},t)$. The transverse dynamic field components of $\boldsymbol{h}(\boldsymbol{r},t)$, h_y and h_z, have the same form as $m_{y,z}$ and may be written as

$$h_{y,z} = h_{yo,zo}(z)\exp\{i[\boldsymbol{k}\cdot\boldsymbol{r} - \omega(k)t]\}. \tag{4}$$

The dynamic field $\boldsymbol{h}$ is the total dynamic Maxwellian field obtained self consistently, along with $\boldsymbol{m}$, from Eq. (3) and Maxwell's equations. In the present context, $\boldsymbol{h}$ may also be viewed as the dipole field generated by the dynamic magnetization $\boldsymbol{m}(\boldsymbol{r},t)$ inside the film. One does not, in the DE approach, include an explicit h_z demagnetizing field term $-4\pi m_z$. The equivalent effect of such a field comes out of the electromagnetic boundary value problem analysis.

The inclusion of anisotropy terms in the dynamic response for spin waves and magnetostatic waves has been discussed by many authors. Working equations in specific form for the uniaxial and cubic anisotropies contained in Eq. (1) are developed in Appendix A. With anisotropy and first order dynamic fields taken into account, the important result is a total effective field $\boldsymbol{H}$ in the $\boldsymbol{x}$–$\boldsymbol{y}$–$\boldsymbol{z}$ precession frame which is given by

$$\boldsymbol{H} = H_S\boldsymbol{e}_x + \boldsymbol{h} + \boldsymbol{A}\cdot\boldsymbol{m}. \tag{5}$$

The static effective field H_S in Eq. (5) is given by

$$H_S = H_0\cos(\Theta-\Phi) + \frac{2K_U}{M_s}\cos^2\Phi - \frac{K_1}{M_s}\sin^2(2\Phi). \tag{6}$$

The matrix $\boldsymbol{A}$ in Eq. (5) is given by

$$\boldsymbol{A} = \begin{pmatrix} 0 & \left[-\frac{K_U}{M_s^2}\sin(2\Phi) - \frac{3K_1}{2M_s^2}\sin(4\Phi)\right] & 0 \\ 0 & \left[\frac{2K_U}{M_s^2}\sin^2(\Phi) + \frac{K_1}{M_s^2}\left[\sin^2(2\Phi) - 2\cos^2(2\Phi)\right]\right] & 0 \\ 0 & 0 & -\frac{2K_1}{M_s^2} \end{pmatrix}. \tag{7}$$

The above relations are valid subject to the static equilibrium condition connecting the applied static external field H_0, the external field angle Θ, and the magnetization angle Φ, given by

$$H_0 \sin(\Theta - \Phi) - \frac{K_U}{M_s}\sin(2\Phi) - \frac{K_1}{2M_s}\sin(4\Phi) = 0. \tag{8}$$

They are also specific to the form of the anisotropy given in Eq. (1). Equivalent free energy expressions, such as a uniaxial term of the form $(K_U/M_s^2)(M_X^2 + M_Y^2)$, for example, would change the specific form of both H_S and A. The overall effective fields which appear in the torque equation, Eq. (3), however, do not change. The physical response, of course, cannot depend on the choice of the form used for the anisotropy energy.

Eq. (8) reduces to well known conditions for static equilibrium in the cases of pure uniaxial or pure cubic anisotropy. In the case of pure uniaxial anisotropy with $K_1 = 0$, $K_U > 0$, and $\Theta = 90°$, for example, the parallel alignment of M_s with H_0 along the hard y-axis can occur only for $H_0 > 2K_U/M_s$. The parameter $H_U = 2K_U/M_s$ represents a uniaxial anisotropy field. As already indicated, H_U for barium ferrite at room temperature is approximately 16 kOe. In the case of pure cubic anisotropy, with $K_U = 0$, $K_1 > 0$, and $\Theta = 45°$, the parallel alignment of M_s with H_0 along the hard 45° axis or crystallographic [110] direction can occur only for $H_0 > 2K_1/M_s$. The parameter $H_A = 2K_1/M_s$ represents a cubic anisotropy field. For bulk single crystal iron, H_A at room temperature is approximately +600 Oe and corresponds to easy axes along the X- and Y-axes in Fig. 2, or the [100] directions in the crystal. For yttrium iron garnet, K_1 at room temperature is negative and H_A is approximately −86 Oe. This corresponds to an easy axis along the [111] crystallographic direction in the crystal. These anisotropy field parameters were introduced above and the values just cited are listed in Table 1.

In general, for any finite value of H_0, and a field direction not along a principal direction such as [100], [110], or [111], M_s will not be parallel to H_0. However, in the limit of large fields, the direction of M_s will approach that of the field. When H_0 is sufficiently large and at $\Theta = 45°$ for YIG or IRON materials, or at $\Theta = 90°$ for HEX materials, M_s will be co-linear with H_0. The stiffness field cases given at the bottom of Table 1 correspond to such co-linear situations. These cases will be used for the numerical results to be presented in subsequent sections.

Eqs. (2)–(7) lead to a relatively simple connection between the transverse components of m and of h

$$\begin{pmatrix} 4\pi m_y \\ 4\pi m_z \end{pmatrix} = \begin{pmatrix} \kappa_\alpha & -i\nu \\ i\nu & \kappa_\beta \end{pmatrix} \begin{pmatrix} h_y \\ h_z \end{pmatrix}. \tag{9}$$

The $\kappa_{\alpha,\beta}$ and ν parameters represent susceptibility functions

$$\kappa_\alpha = \frac{\Omega_\alpha}{\Omega_\alpha \Omega_\beta - \Omega^2}, \tag{10}$$

$$\kappa_\beta = \frac{\Omega_\beta}{\Omega_\alpha \Omega_\beta - \Omega^2}, \tag{11}$$

$$\nu = \frac{\Omega}{\Omega_\alpha \Omega_\beta - \Omega^2}. \tag{12}$$

The Ω and $\Omega_{\alpha,\beta}$ represent reduced frequency parameters

$$\Omega = \frac{\omega/\gamma}{4\pi M_s}, \tag{13}$$

$$\Omega_{\alpha,\beta} = \frac{H_{\alpha,\beta}}{4\pi M_s}. \tag{14}$$

The H_α and H_β field parameters, in turn, represent effective stiffness fields which come from the H_S expression and the terms in the $\boldsymbol{A}$ matrix given above

$$H_\alpha = H_o \cos(\Theta - \Phi) + H_U \cos^2\Phi + H_A\left[1 - \tfrac{1}{2}\sin^2(2\Phi)\right], \tag{15}$$

$$H_\beta = H_o \cos(\Theta - \Phi) + H_U \cos(2\Phi) + H_A \cos(4\Phi). \tag{16}$$

The above expressions follow from Eq. (3), in combination with the dynamic magnetization response $\boldsymbol{m}$ of Eq. (2), the dynamic Maxwellian field $\boldsymbol{h}$, and the total effective field specified through Eqs. (5)–(7). Note that all of the above is contingent on values of the magnetization angle Φ for given values of H_o and Θ which satisfy the static equilibrium condition of Eq. (8). Note also that Eqs. (9)–(16) parallel, in large measure, the corresponding equations for the isotropic film case given in Ref. [1]. In the zero anisotropy limit, with $H_U = 0$, $H_A = 0$, and $\Phi = \Theta$, both H_α and H_β reduce to the static external field H_o and the equations given above reduce to the corresponding expressions in Refs. [1,7]. Physically, H_α corresponds to a stiffness field for the tipping of the magnetization vector $\boldsymbol{M}$ away from the equilibrium x-axis and toward the z-axis, or out of the plane of the film. The stiffness field H_β corresponds to the stiffness field for a tipping of the magnetization vector $\boldsymbol{M}$ away from the equilibrium x-axis and toward the y-axis, in the plane of the film.

Note that Eq. (9), with the $\kappa_{\alpha,\beta}$ and ν parameters as defined, is explicitly for an assumed $e^{-i\omega t}$ time dependence. Sign inconsistencies are pervasive in the literature. Lax and Button [57], for example, write Eq. (1) without the minus sign, use an $e^{+i\omega t}$ time dependence, and obtain the same susceptibility connection given above.

2.3. Electromagnetic boundary value problem

The remainder of the formal analysis parallels the development in Ref. [1] for isotropic materials, with the replacement of the Damon and Eshbach reduced field parameter Ω_H by $\Omega_{\alpha,\beta}$ as needed. The first step in the analysis is in the use of the Maxwell equation for $\nabla \times \boldsymbol{h}(\boldsymbol{r},t)$ in the so-called 'magnetostatic' approximation, discussed in Appendix A of Ref. [1]. In this approximation, the $\nabla \times \boldsymbol{h}$ Maxwell equation simply reduces to $\nabla \times \boldsymbol{h} = 0$. This condition is satisfied automatically by expressing $\boldsymbol{h}(\boldsymbol{r},t)$ in terms of a scalar potential $\psi(\boldsymbol{r})$ according to $\boldsymbol{h}(\boldsymbol{r},t) = \nabla\psi(\boldsymbol{r})e^{-i\omega t}$. The problem is now reduced to finding the propagating normal mode solutions for the scalar potential $\psi(\boldsymbol{r})$ which satisfy the $\nabla \cdot \boldsymbol{b} = \nabla \cdot (\boldsymbol{h} + 4\pi\boldsymbol{m}) = 0$ condition, subject to the usual boundary conditions on $\boldsymbol{h}$ and $\boldsymbol{b}$ at the film surfaces. The power of the Damon–Eshbach formulation is in the use of scalar potentials to obtain relatively simple working equations for mode frequencies and profiles.

One sets up trial scalar potential functions in the same way as for the isotropic film. These functions are defined the same way, and follow the same notation used in Refs. [1,7]. The scalar potential function inside the film, corresponding to $|z| < S/2$, is denoted as $\psi^i(\boldsymbol{r})$. Outside or external to the film, corresponding to $|z| > S/2$, the scalar potential is $\psi^e(\boldsymbol{r})$. These scalar potential functions are taken as separable and of the form

$$\psi^i(x,y,z) = X(x)Y(y)Z^i(z) \tag{17}$$

and

$$\psi^e(x,y,z) = X(x)Y(y)Z^e(z). \tag{18}$$

The $X(x)$ and $Y(y)$ functions are common to both $\psi^i(\boldsymbol{r})$ and $\psi^e(\boldsymbol{r})$. The $X(x)$, $Y(y)$, and $Z(z)$ notation here has nothing to do with the X-, Y-, and Z-axes in the sample frame discussed above. These function labels simply parallel the DE notation used in Refs. [1,7]. These functions give an in-plane propagating wave at frequency ω with an in-plane wave vector $\boldsymbol{k}$ as defined in Fig. 2

$$\boldsymbol{k} = \begin{pmatrix} k_x \\ k_y \\ 0 \end{pmatrix} = k \begin{pmatrix} \cos\phi \\ \sin\phi \\ 0 \end{pmatrix}. \tag{19}$$

The X and Y functions may be written as

$$X(x) = e^{ik_x x} = e^{i(k\cos\phi)x} \tag{20}$$

and

$$Y(y) = e^{ik_y y} = e^{i(k\sin\phi)y}. \tag{21}$$

The parameter k represents the wave number for the in-plane propagation. As in Ref. [1], the relative sizes of k_x and k_y and the corresponding propagation angle ϕ, as well as the sign of k_y, will play important roles in determining the nature of the normal modes.

The $Z^i(z)$ and $Z^e(z)$ functions must conform to basic symmetry considerations

$$Z^i(z) = a\sin(k_z^i z) + b\cos(k_z^i z) \quad (|z| < S/2), \tag{22}$$

$$Z^e(z) = c\,e^{-k_z^e z} \quad (z > +S/2), \tag{23}$$

$$Z^e(z) = d\,e^{+k_z^e z} \quad (z < -S/2). \tag{24}$$

Note that the in-plane propagating wave form of the normal modes and the requirement that $\boldsymbol{h}$ and $\boldsymbol{m}$ decay to zero for $|z| \gg S/2$ require that k_x, k_y, and k_z^e be purely real and that k_z^e also be positive. As discussed in Ref. [1], there are no such restrictions on k_z^i. Both real and imaginary values for k_z^i are allowed. Real values for k_z^i correspond to harmonic solutions for $Z^i(z)$ inside the film. These solutions correspond to the volume modes discussed in Ref. [1]. Imaginary values for k_z^i will correspond to $Z^i(z)$ solutions which grow or decay exponentially with distance into the film interior from one surface or the other. These solutions correspond to the surface mode obtained in Ref. [1].

The $\nabla\cdot\boldsymbol{b} = \nabla\cdot(\boldsymbol{h} + 4\pi\boldsymbol{m}) = 0$ condition inside the film gives a relatively simple differential equation for $\psi^i(\boldsymbol{r})$

$$\left[\frac{\partial^2}{\partial x^2} + (1+\kappa_\alpha)\frac{\partial^2}{\partial y^2} + (1+\kappa_\beta)\frac{\partial^2}{\partial z^2}\right]\psi^i(x,y,z) = 0. \tag{25}$$

This is Laplace's equation with additional terms involving κ_α and κ_β. In the limit of no anisotropy, Eq. (25) reduces to Eq. (15) in Ref. [1]. Outside the film, one has $\boldsymbol{m} = 0$. The corresponding $\nabla\cdot\boldsymbol{b} = \nabla\cdot\boldsymbol{h} = 0$ condition gives Laplace's equation for $\psi^e(\boldsymbol{r})$

$$\left(\frac{\partial^2}{\partial x^2} + \frac{\partial^2}{\partial y^2} + \frac{\partial^2}{\partial z^2}\right)\psi^e(x,y,z) = 0. \tag{26}$$

The above two equations, along with the functional dependences for $\psi^i(\boldsymbol{r})$ and $\psi^e(\boldsymbol{r})$ given through Eqs. (17)–(24), immediately yield two connective equations between the wave number parameters k_x, k_y, and k_z^i

$$k_x^2 + (1+\kappa_\alpha)k_y^2 + (1+\kappa_\beta)(k_z^i)^2 = 0, \tag{27}$$

$$k_x^2 + k_y^2 - (k_z^e)^2 = 0. \tag{28}$$

As did Eq. (17) in Ref. [1], Eq. (27) defines conditions for real or imaginary values of k_z^i and the corresponding frequency limits for the volume and surface modes. Eq. (27), however, is more complicated than the counterpart Eq. (17) in Ref. [1]. The surface and volume mode frequency limits which derive from Eq. (27) will be considered in detail shortly. Eq. (28), which is the same as Eq. (18) in Ref. [1], shows that k_z^e, the exponential $1/e$ decay rate for $\psi^e(\boldsymbol{r})$ outside the film, is equal to the propagation wave number $k = (k_x^2 + k_y^2)^{1/2}$.

The remaining steps in the formal analysis, as in the isotropic film case, are straightforward but tedious. One applies the usual electromagnetic boundary conditions which yield connections between the a, b, c, and d coefficients of Eqs. (22)–(24)

$$a = \frac{c-d}{2}\frac{e^{-k_z^e S/2}}{\sin(k_z^i S/2)}, \tag{29}$$

$$b = \frac{c+d}{2}\frac{e^{-k_z^e S/2}}{\cos(k_z^i S/2)}, \tag{30}$$

and

$$\frac{(c-d)}{(c+d)} = \frac{\nu k_y}{(1+\kappa_\beta)k_z^i \cot(k_z^i S/2) + k_z^e} = -\frac{(1+\kappa_\beta)k_z^i \tan(k_z^i S/2) - k_z^e}{\nu k_y}. \tag{31}$$

The second equality in Eq. (31), in combination with the relation $k_y = k\sin\phi$, yields a general connective equation between the mode frequency and the various wave number parameters

$$(k_z^e)^2 - (k_z^i)^2(1+\kappa_\beta)^2 - \nu^2 k^2 \sin^2\phi + 2k_z^i k_z^e(1+\kappa_\beta)\cot(k_z^i S) = 0. \tag{32}$$

Eq. (32) constitutes the operational dispersion equation for the magnetostatic modes for the anisotropic film. Eq. (32) is identical to Eq. (22) in Ref. [1], except for the appearance of κ_β in place of κ. The dispersion character of Eq. (32) is made evident by noting that the k_z^i and k_z^e parameters are related to the propagation wave number k through Eqs. (19), (27) and (28), by

$$k_z^i = \pm\sqrt{-\frac{1+\kappa_\alpha \sin^2\phi}{1+\kappa_\beta}}\cdot k \tag{33}$$

and

$$k_z^e = k. \tag{34}$$

Recall that k_z^e and k are real and positive. Recall also that the mode frequency ω, or equivalently, the normalized frequency Ω, is imbedded in the $\kappa_{\alpha,\beta}$ and ν parameters. Considered together, Eqs. (32)–(34) constitute a general dispersion equation for the various normal mode magnetostatic waves of an in-plane magnetized thin film. Eq. (33) is the anisotropic counterpart to Eq. (23) in Ref. [1]. The specific placements of the κ_α and the κ_β terms in Eqs. (32) and (33) lead to the important changes due to anisotropy.

Although the dispersion conditions implicit in Eqs. (32)–(34) are more complicated than for isotropic films, several of the functional dependences are similar. First, note that neither the z-dependence in the scalar potential, defined through the $Z^i(z)$ function in Eq. (22) with coefficients given by Eqs. (29)–(31), nor the dispersion condition of Eq. (32), are affected by a change in sign for k_z^i. In the volume mode analysis to follow, under conditions for which the square root argument in Eq. (33) is positive, k_z^i will be taken as positive. The special case in which the square root argument in Eq. (33) is negative leads to an imaginary k_z^i and the so-called surface mode. Note also, as in the isotropic case, that a change in the sign of the propagation angle ϕ can change the normal mode solution through the νk_y terms in Eq. (31). As in Ref. [1], this result has important consequences in terms of nonreciprocal mode behavior.

In addition to the consideration of dispersion properties, Ref. [1] contained extensive discussions of mode polarizations and mode profiles for both volume and surface modes in isotropic films. The basic results given in

Ref. [1] also apply here. The most important of these results are (1) the standing wave nature of the volume modes and (2) the decay in the dynamic response as one moves into the film interior from one or the other film surface which characterizes the surface mode. As evident from the previous two subsections, the key factor which distinguishes between these two types of modes is the real or imaginary status of k_z^i. The separation between the volume and surface modes is quite clear for isotropic films and anisotropic YIG films. This will not be the case for IRON and HEX films.

2.4. Characteristic equations and frequency regimes

Eqs. (32)–(34) can be reduced to a transcendental dispersion equation connecting the mode frequency, the in-plane wave number k, and the propagation angle ϕ. With k_z^i taken as positive, according to the '+' multiplier in front of the square root in Eq. (33), the first part of this general dispersion equation is given by

$$(1+\kappa_\beta)^2\left(-\frac{1+\kappa_\alpha\sin^2\phi}{1+\kappa_\beta}\right)+\nu^2\sin^2\phi-1-2(1+\kappa_\beta)\sqrt{-\frac{1+\kappa_\alpha\sin^2\phi}{1+\kappa_\beta}}\cot(k_z^i S)=0. \tag{35}$$

As will be discussed shortly, Eq. (35) determines the allowed values of k_z^i as a function of frequency. The second part of the dispersion comes from the connection between k_z^i and the propagating wave number k through Eq. (33), again taken with the '+' sign. Note that the square root expression in Eq. (33) also appears as a multiplier of the $\cot(k_z^i S)$ in Eq. (35). This means that the sign of the expression under the square root in both Eqs. (33) and (35) determines whether k_z^i at a given field, frequency, and propagation angle will be real and positive, or imaginary. In terms of the reduced frequency and field parameters defined above, the square root expression in Eqs. (33) and (35) can be written as

$$-\frac{1+\kappa_\alpha\sin^2\phi}{1+\kappa_\beta}=\frac{\Omega^2-\Omega_\alpha(\Omega_\beta+\sin^2\phi)}{\Omega_\beta(\Omega_\alpha+1)-\Omega^2}=\Pi. \tag{36}$$

The middle part of Eq. (36) has been written in terms of the reduced frequency parameter $\Omega=\omega/\gamma 4\pi M_s$. In parallel with the discussion in Ref. [1], the condition for real k_z^i and, hence, volume modes, is that Π be positive. One then obtains k_z^i for any given wave number k and propagation angle ϕ according to $k_z^i=\Pi^{1/2}k$. In the case of isotropic films, with $H_\alpha=H_\beta=H_0$ and $\Omega_\alpha=\Omega_\beta=\Omega_H=H_0/4\pi M_s$, this condition is quite simple and leads to the upper and lower frequency limits of $\Omega_B=[\Omega_H(\Omega_H+1)]^{1/2}$ and $\Omega_A=[\Omega_H(\Omega_H+\sin^2\phi)]^{1/2}$, respectively, for volume modes. In the isotropic limit, therefore, the volume mode band is the same as the bulk spin wave band, $\Omega_B<\Omega<\Omega_H$, for $\phi=0$ and collapses to zero width at $\Omega=\Omega_B$ for $\phi=90°$. These points were discussed at length in Ref. [1].

Note also that k_z^i occurs in the above dispersion equation only in combination with the film thickness S, as $k_z^i S$. The wave number–thickness products $k_z^i S$ and kS will turn out to be useful reduced wave number parameters for the graphical presentation and discussion of dispersion properties.

Because of the specific placements of the Ω_α and Ω_β parameters in the numerator and denominator expressions in the middle part of Eq. (36), along with the fact that the relative sizes of Ω_α and Ω_β can vary according to the nature of the anisotropy and the orientation of the static magnetization vector $\boldsymbol{M}_s$ relative to the anisotropy axes as shown in Fig. 1, the volume mode band ϕ-profiles become more complicated for anisotropic films. The effect of anisotropy on the volume mode bands as well as the volume mode dispersion curves for YIG, IRON, and HEX materials will be examined in detail in the next three sections. The remaining discussion in this section is limited to several observations based on the form of Eq. (36).

First, note that the volume mode band limits are determined by the separate numerator and denominator

terms in the middle part of Eq. (36). In parallel with the formalism in Ref. [1], let the denominator determined volume mode band limit be specified by

$$\Omega_B = \sqrt{\Omega_\beta(\Omega_\alpha + 1)}\,, \tag{37}$$

and let the numerator limit be specified as

$$\Omega_A = \sqrt{\Omega_\alpha\left(\Omega_\beta + \sin^2\phi\right)}\,. \tag{38}$$

For isotropic films, $\Omega_\alpha = \Omega_\beta = \Omega_H$ is satisfied. In this limit, Ω_A is always less than Ω_B for ϕ values below 90° and equal to Ω_B at $\phi = 90°$. For anisotropic films, Ω_A may fall below or above Ω_B, depending on the relative sizes of Ω_α and Ω_β.

Consider first the case in which $\Omega_\beta > \Omega_\alpha$ is satisfied. In this situation, Ω_A will always be below Ω_B. For $\phi = 0$, one has $\Omega_B = [(\Omega_\alpha + 1)\Omega_\beta]^{1/2}$ and $\Omega_A = (\Omega_\alpha\,\Omega_\beta)^{1/2}$. For $\phi = 90°$, Ω_A increases to $[\Omega_\alpha(\Omega_\beta + 1)]^{1/2}$, a value still somewhat below Ω_B. The basic volume mode band in this case is similar to the band for the isotropic film, except for a surviving band width even at $\phi = 90°$. As will be considered in the next section, thin film materials with YIG properties have volume mode bands which conform to this description when magnetized in an in-plane hard direction. The volume mode band limits are specified, in this case, according to

$$\Omega_\beta(\Omega_\alpha + 1) > \Omega^2 > \Omega_\alpha\left(\Omega_\beta + \sin^2\phi\right) \quad (\Omega_\beta > \Omega_\alpha, 0 < \phi < 90°). \tag{39}$$

Eq. (39) is the anisotropic version of Eq. (27) in Ref. [1].

The situation is somewhat more interesting in the case in which $\Omega_\alpha > \Omega_\beta$ is satisfied. In this situation, Ω_A will be below Ω_B only for a propagation angle ϕ which is below a critical value ϕ_x defined by $\Omega_\beta = \Omega_\alpha \sin^2\phi_x$. For propagation angles greater that ϕ_x, the volume mode band becomes inverted. Propagation at $\phi = \phi_x$ corresponds, therefore, to a crossover situation. The volume mode frequency limits are the same as in Eq. (39) for ϕ below the crossover point and inverted above crossover

$$\Omega_\beta(\Omega_\alpha + 1) > \Omega^2 > \Omega_\alpha\left(\Omega_\beta + \sin^2\phi\right) \quad (\Omega_\alpha > \Omega_\beta, 0 < \phi < \phi_x), \tag{40}$$

$$\Omega_\alpha\left(\Omega_\beta + \sin^2\phi\right) > \Omega^2 > \Omega_\beta(\Omega_\alpha + 1) \quad (\Omega_\alpha > \Omega_\beta, \phi_x < \phi < 90°). \tag{41}$$

The volume mode band above the crossover point in this case is very different from the band for the isotropic film. This situation occurs for IRON materials magnetized in-plane and along a hard [110] direction, and for HEX materials magnetized in-plane and at 90° to the uniaxial easy axis. These cases will be considered explicitly in Section 4, 5, respectively.

Return now, as this section is concluded, to consider Eq. (36) under conditions for which Π is negative. In parallel with the results in Ref. [1], a negative value of Π corresponds to purely imaginary values for k_z^i and one may describe the $Z^i(z)$ response profiles inside the film in terms of exponential functions with a decay parameter $\kappa_z^i = -ik_z^i$. Such profiles correspond to the surface mode. As for isotropic films, the anisotropic film conditions which yield negative values of Π, and hence, the surface mode, involve propagation angles greater that some critical angle ϕ_c and mode frequencies within a second band which falls above the volume mode band. This critical angle also has effects on the nature of the actual volume mode dispersion curves which is similar to the result for isotropic films.

Under conditions for which there are volume mode band crossover and inversion effects at the crossover critical angle $\phi_x = \sin^{-1}(\Omega_\beta/\Omega_\alpha)^{1/2}$ through the $\Omega_\alpha > \Omega_\beta$ condition considered above, there are also significant effects for the surface mode behavior. The critical angle ϕ_c in anisotropic films is generally less than ϕ_x. Under conditions for which the propagation angle is greater than ϕ_x, and below a *third* critical angle ϕ_p, the surface mode is found to have re-entrant properties. The third critical angle ϕ_p is found for HEX materials. For propagation angles greater than ϕ_p, the surface mode band merges with the inverted volume mode band. The basic result is a limited sector of propagation angles defined by $\phi_c < \phi < \phi_p$ for which the surface mode is allowed. These properties will be examined in the subsequent sections.

3. Results for YIG films

One example of the effects of anisotropy and the role of Ω_α and Ω_β differences is obtained for material parameters applicable to YIG and a moderate applied external field H_0 sufficient to align the static magnetization vector $\boldsymbol{M}_s$ along or nearly along the field direction. Consider a YIG film with a saturation induction $4\pi M_s = 1750$ G and a cubic anisotropy field $H_A = -86$ Oe, with an external magnetic field $H_0 = 1000$ Oe applied in-plane at some angle Θ relative to the X-axis and the [100] crystallographic direction in the film. Under the assumption of a film which is uniformly magnetized in an in-plane [100] direction prior to the application of the field, the small size of H_A relative to H_0 leads to an approximate lineup of $\boldsymbol{M}_s$ with $\boldsymbol{H}_0$ and an $\boldsymbol{M}_s$ direction at $\Phi \approx \Theta$. For $\boldsymbol{M}_s$ and $\boldsymbol{H}_0$ in the (100) film plane, and under the YIG conditions specified above, the $|\Phi - \Theta|$ difference remains below 1° or so for all field directions. This condition will be termed 'quasi-lineup'. As a starting point for the YIG materials discussion, consider the variation of the two effective stiffness fields H_α and H_β given through Eqs. (15) and (16) for the rotation of the static magnetic field from $\Theta = 0°$ to 90°. For this YIG scenario, H_U is set to zero, H_A is set to -86 Oe, and quasi-lineup with Φ equal to Θ is assumed. The results are shown in Fig. 3. The horizontal axis in Fig. 3 gives the field angle Θ. The vertical axis shows the computed values of H_α and H_β. The stiffness field for out-of-plane tipping, H_α, ranges from 914 Oe at 0°, up to a peak value of 957 Oe at 45°, and back to 914 Oe at 90°. The stiffness field for in-plane tipping, H_β, is the same as H_α at 0° and 90°, but reaches a significantly higher peak value of 1086 Oe at 45°.

Note that one would expect H_α and H_β to be the same at 0° and 90° because of symmetry. While the H_α and H_β represent stiffness fields for out-of-plane and in-plane tipping of the magnetization vector, respectively, they do not include thin film demagnetizing effects. With such effects neglected, in-plane or out-of-plane tipping away from [100] and [010] directions are energetically equivalent. The 914 Oe value is below the 1000 Oe applied static field because the [100] and [010] directions are hard directions and the tippings are more-or-less toward the easy [111] direction.

The situation is different at 45°. Here, the value of H_α is smaller than the 1000 Oe static field by 43 Oe and the value of H_β is larger by 86 Oe. These changes are intuitively correct. Out-of-plane tipping is towards each [111] direction, so that H_α should be smaller than 1000 Oe. In-plane tipping, on the other hand, is away from [111], so that H_β should be larger than 1000 Oe. At $\Theta = \Phi = 45°$, Eqs. (15) and (16) give $H_\alpha = H_0 + H_A/2 = 957$ Oe and $H_\beta = H_0 - H_A = 1086$ Oe. These are the values listed in column 2 of Table 1.

Recall that the reduced stiffness frequencies Ω_α and Ω_β are just the corresponding fields divided by the saturation induction $4\pi M_s$. Given Ω_α and Ω_β, the band limit frequencies Ω_B and Ω_A may be immediately obtained from Eqs. (37) and (38). It is clear from Fig. 3 that for the YIG materials under consideration here, the

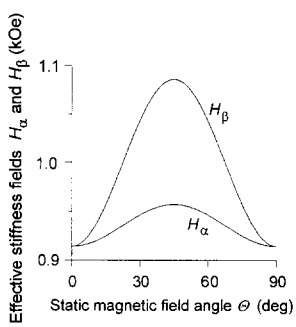

Fig. 3. Variation of the two effective stiffness fields H_α and H_β with the angle Θ between the in-plane cubic [100] direction and the direction of a 1000 Oe in-plane static magnetic field for a YIG film with a first order magnetocrystalline anisotropy field H_A of -86 Oe, under the assumption of quasi-lineup of the static magnetization vector $\boldsymbol{M}_s$ with the magnetic field.

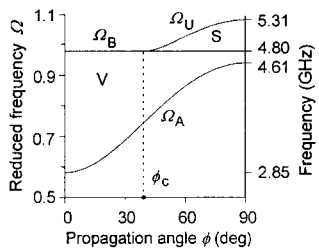

Fig. 4. Theoretical volume mode and surface mode bands as a function of in-plane propagation angle ϕ for a (100) plane YIG film with cubic magnetocrystalline anisotropy. The Ω_A curve shows the bottom and the Ω_B curve shows the top of the volume mode band. The curve labeled Ω_U shows the top of the surface mode band which emerges from the top of the volume mode band at a critical propagation angle $\phi_c \approx 39.3°$. The labels V and S designate the volume and surface mode bands, respectively. The curves are based on values for the static in-plane field H_o, the film saturation induction $4\pi M_s$, a cubic anisotropy field H_A, and a field angle Θ relative to the [100] cubic axis of 1000 Oe, 1750 G, −86 Oe, and 45°, respectively. The scale on the right side vertical axis gives limit frequency values in GHz.

condition $H_\alpha \leq H_\beta$ and the corresponding frequency condition $\Omega_\alpha \leq \Omega_\beta$ are always satisfied. This means that the volume mode band limits will also satisfy the condition $\Omega_B \geq \Omega_A$ for all values of the propagation angle ϕ.

3.1. Volume modes

Fig. 4 shows a plot of the two volume mode band frequency limits Ω_A and Ω_B as a function of the propagation angle ϕ for the YIG parameters and the $\Theta = 45°$ hard direction 1000 Oe field situation introduced above. The left-side vertical scale gives the reduced frequencies and the right-side vertical scale gives actual frequencies in GHz. The curves which correspond to the Ω_A and Ω_B frequencies are indicated. The region between the Ω_A and Ω_B curves is labeled V to indicate the volume mode band.

Fig. 4 also shows a third curve, labeled Ω_U, which emerges from the top of the volume mode band at $\phi = \phi_c \approx 39°$. This ϕ_c is the critical propagation angle for the surface mode and for a change in character for the volume modes as well. These critical angle effects, while similar to the situation for isotropic films, have important differences for anisotropic materials which will be treated in detail as the discussion of YIG, IRON, and HEX materials unfolds. The region between the Ω_U and Ω_B curves in Fig. 4 is labeled S to designate the surface mode band. The surface mode for YIG films will be considered in Section 3.2.

The qualitative nature of the volume mode band in Fig. 4 is similar to the volume mode band shown in Fig. 2 of Ref. [1] for isotropic films. The top of the band at $\Omega = \Omega_B$ is independent of the propagation angle. The bottom of the band defined by Ω_A starts out well below Ω_B for $\phi = 0$ and curves upward toward Ω_B as ϕ increases to 90°. The main difference between this YIG film magnetized in a hard direction and an isotropic film is that a small but nonzero gap still remains between Ω_A and Ω_B at $\phi = 90°$. In the isotropic case, the fact that Ω_α and Ω_β are always equal causes the width of the band to collapse to zero at $\phi = 90°$.

As was the case for Fig. 2 in Ref. [1], it is important to realize that each propagation angle value in Fig. 4 corresponds to an infinite manifold of volume mode dispersion curves of frequency vs. wave number, all contained between the frequency limits indicated. The solutions for and the behavior of these dispersion curves for the specific YIG parameters under consideration here correspond closely to the discussion in Section 3 of Ref. [1]. The discussion below is an abbreviated version of the discussion of Section 3 in Ref. [1], with suitable modifications to include anisotropy. The details of the analysis will also be important for the discussion of the surface mode for YIG materials in Section 3.2 and for the treatments of IRON and HEX materials in Sections 4 and 5.

Solutions for the volume mode frequencies versus wave number in a Ω versus k format at different values of the propagation angle ϕ are obtained from Eqs. (33) and (35). As already indicated, one may take the positive square root in Eq. (33) and write the connection between k and k_z^1 as $k = +k_z^1/\Pi$, with Π from Eq.

(36). In parallel with the discussion at the end of Section 3 in Ref. [1], the volume mode dispersion branch solutions may be written in terms of two equations

$$\cot\left(k_z^i S\right) = G_a(\Omega)\frac{1}{2}\left[\frac{\left(\Omega^2 - \Omega_A^2\right) - \left(\Omega_B^2 - \Omega^2\right) - \sin^2\phi}{\sqrt{\left(\Omega_B^2 - \Omega^2\right)\left(\Omega^2 - \Omega_A^2\right)}}\right] \tag{42}$$

and

$$k = \sqrt{\frac{\Omega_B^2 - \Omega^2}{\Omega^2 - \Omega_A^2}}\, k_z^i. \tag{43}$$

Solutions to Eqs. (42) and (43) are, of course, limited to the frequency range $\Omega_A < \Omega < \Omega_B$. Keep in mind that the discussion here is for volume modes in YIG for the static applied field $\boldsymbol{H}_0$ at $\Theta = 45°$ and the static magnetization $\boldsymbol{M}_s$ at $\Phi = 45°$ as well. Eqs. (42) and (43) correspond to Eqs. (34) and (35) in Ref. [1].

From the denominator term on the right-hand side expression of Eq. (42), it is clear that $G_a(\Omega)$ diverges as Ω approaches either Ω_B or Ω_A from within the band. The sign of the divergence is determined by the sign of the numerator at these two band limits. In parallel with the discussion in Ref. [1], as long as the propagation angle ϕ is sufficiently small, the divergence will be to $+\infty$ for $\Omega \to \Omega_B$ and to $-\infty$ for $\Omega \to \Omega_A$. However, when ϕ becomes sufficiently large such that

$$\sin^2\phi > \Omega_B^2 - \Omega_A^2(\phi) \tag{44}$$

is satisfied, the divergence will be *negative* at both band limits. As discussed in Ref. [1] for the isotropic case, this critical angle effect has important consequences for the shapes of the volume mode dispersion curves. The $\Omega_A(\phi)$ term in Eq. (44) is written to emphasize the fact that Ω_A is also ϕ-dependent. Eq. (44) yields a critical angle given by

$$\phi_c = \sin^{-1}\sqrt{\frac{\Omega_\beta}{1 + \Omega_\alpha}}\,. \tag{45}$$

For the YIG parameters cited above, ϕ_c is 39.3°. In the isotropic limit with $\Omega_\alpha = \Omega_\beta = \Omega_H = H_0/4\pi M_s$, this is the same critical angle given in Ref. [1]. It is also the critical angle for the surface mode, to be considered shortly.

Return to the volume mode dispersion solutions based on Eqs. (42) and (43). The left-hand side of Eq. (42) is simply $\cot(k_z^i S)$. This function diverges to $\pm\infty$ at $k_z^i S = 0, \pi, 2\pi, \ldots$. It is the match up of the intersection of the $G_a(\Omega)$ at particular values of Ω within the band with the various $\cot(k_z^i S)$ branch curves which determines the applicable values of k_z^i at that frequency. Once these k_z^i values are determined, the wave number k values are obtained from Eq. (43). Each $\cot(k_z^i S)$ branch curve, therefore, will yield one dispersion curve of Ω versus k.

The nature of these solutions as well as the critical angle effect can be visualized with the help of Fig. 5, which shows a plot of the first three branch curves of $\cot(k_z^i S)$ vs. $k_z^i S$, shown by the solid lines labeled $n = 1$, 2, and 3, and horizontal dashed lines across these branch curves which correspond to the numerical value of $G_a(\Omega)$ for several values of the reduced frequency Ω between Ω_B and Ω_A at $\phi = 0$. The applicable Ω values are indicated beside each cut. All parameters are the same as used for the band diagram of Fig. 4. Note that the horizontal cuts range from negative values of G_a for reduced frequencies very close to Ω_A to positive values for Ω very close to Ω_B. The corresponding dispersion solutions for $k_z^i S$ as a function of Ω are indicated by the intersection points between the $\cot(k_z^i S)$ branch curves and the cuts. As Ω moves from Ω_B to Ω_A, the G_a cut moves from $+\infty$ to $-\infty$, and $k_z^i S$ moves from $(n-1)\pi$ to $n\pi$ for a given branch n. For the first branch, for example, $k_z^i S$ ranges from zero to π as Ω ranges from Ω_B down to Ω_A. For the second branch, $k_z^i S$ ranges from π to 2π as Ω ranges from Ω_B down to Ω_A, and so forth. This means that the standing wave pattern

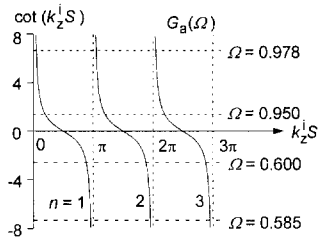

Fig. 5. Plot of the first three branch curves of the function $\cot(k_z^i S)$ vs. $k_z^i S$, shown by the solid lines labeled $n = 1, 2, 3$, and horizontal cuts across these branch curves which correspond to the $G_a(\Omega)$ function defined in the text for several values of the frequency between the volume mode band limit frequencies Ω_B and Ω_A. The $G_a(\Omega)$ cut values are for a YIG film and are based on values for the static in-plane field H_0, the film saturation induction $4\pi M_s$, the cubic anisotropy field H_A, and the in-plane field angle Θ relative to the in-plane [100] cubic axis of 1000 Oe, 1750 G, −86 Oe, and 45°, respectively, as for Fig. 4. The $G_a(\Omega)$ values are for an in-plane propagation angle ϕ of 0°.

across the thickness of the film for the nth branch evolves from $(n-1)$ half wavelengths to n half wavelengths across the film as one moves from the upper limit frequency Ω_B to the lower limit frequency Ω_A. The first branch, with $n = 1$, starts out as a *z-independent* uniform profile with $k_z^i S = 0$ at $\Omega = \Omega_B$ and ends up at $\Omega = \Omega_A$ with $k_z^i S = \pi$. All higher order branches start out at Ω_B with a nonzero value of $k_z^i S = (n-1)\pi$ and end up at $k_z^i S = n\pi$ for $\Omega = \Omega_A$.

The k_z^i values indicated above convert into actual propagation wave number k values through Eq. (43). Due to the numerator and denominator terms under the square root in Eq. (43), the limiting k values at the $\Omega \to \Omega_B$ and $\Omega \to \Omega_A$ band limits will always be at zero and infinity, respectively. The detailed shapes of the individual dispersion branches, however, will be determined by the various branch intersections described above. Of particular note is the lowest order $n = 1$ branch, for which the branch-cut solution gives $k_z^i S = 0$ in the $\Omega \to \Omega_B$ limit. This limit corresponds to zero values for both k_z^i and the propagation wave number k in the $\Omega \to \Omega_B$ limit. This limit is the usual ferromagnetic resonance mode in thin films for $\Omega = \Omega_B$. The same situation was found for isotropic films. This lowest order dispersion branch, therefore, has special significance for anisotropic films, just as it does for isotropic films. The above limits yield an $n = 1\,\Omega$ versus k dispersion branch which approaches $\Omega = \Omega_B$ at zero k with a nonzero slope. The higher order branches have limiting values of k_z^i in the $\Omega \to \Omega_B$ limit which are nonzero. These dispersion curves approach $\Omega = \Omega_B$ at zero k with a zero slope. These behaviors are discussed in detail in Ref. [1].

It is important to keep in mind that the specific behavior shown in Fig. 5 is for $\phi = 0$, with propagation parallel to the static magnetization direction. The same behavior is found as long as the propagation angle is below the critical angle ϕ_c. For $\phi < \phi_c$, the only new effect is in the increase in the frequency for the bottom of the band, Ω_A. When ϕ exceeds ϕ_c, however, the divergence in G_a in the $\Omega \to \Omega_B$ limit becomes negative instead of positive. The corresponding $k_z^i S$ solution for the $n = 1$ dispersion branch is π rather than zero. The effect of this change is two-fold. First, one no longer has a dynamic response across the film which corresponds to a uniform mode. One has, rather, a standing mode profile of wavelength $2S$ across the film cross section. Second, the $n = 1$ dispersion branch no longer comes into $\Omega = \Omega_B$ with a nonzero slope. The overall effect is that, for propagation angles above the critical angle, all of the volume mode dispersion branches have similar behaviors in the $\Omega \to \Omega_B$ limit, comprised of standing mode profiles with nonzero k_z^i values and zero slopes. These behaviors were discussed at length in Ref. [1]. They will have additional significance for anisotropic films. For the YIG films considered in this section, one has the possibility of no critical angle effect at all. This situation will be considered in Section 3.2. There are further considerations for IRON and HEX films which involve band inversion and re-entrant modes. These effects are considered in Sections 4 and 5.

Turn now to some specific dispersion curve results for YIG films. Fig. 6 shows a series of dispersion curve diagrams for four values of the propagation angle ϕ, at $\phi = 0°$, 30°, 60°, and 90°, and the same parameters used

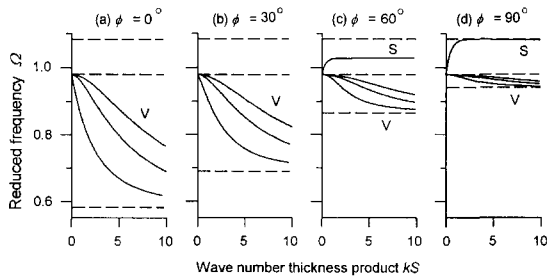

Fig. 6. Dispersion curves of reduced frequency Ω vs. reduced wave number kS for four values of the propagation angle ϕ, as indicated. Each diagram shows a set of three curves, labeled V, which correspond to the three lowest order volume mode dispersion branches. Diagrams (c) and (d), where $\phi > \phi_c = 39.3°$, also show the surface mode dispersion curve, indicated by the S label. The upper and lower volume mode band limit frequencies Ω_B and Ω_A, and the upper surface mode band limit frequency Ω_S for $\phi = 90°$, are shown in each diagram by the horizontal dashed lines. All curves are for a YIG film and are based on values for the static in-plane field H_0, the film saturation induction $4\pi M_s$, a cubic anisotropy field H_A, and a field angle Θ relative to the [100] cubic axis of 1000 Oe, 1750 G, −86 Oe, and 45°, respectively, as for Fig. 4.

for Figs. 3–5. Diagrams (a) and (b) are for ϕ values below and diagrams (c) and (d) are for ϕ values above the critical angle ϕ_c. As for the band limit curves in Fig. 4, the dispersion curves in Fig. 6 are of reduced frequency Ω vs. reduced wave number kS. Each diagram shows a set of three volume mode dispersion curves, labeled V. These curves correspond to the three lowest dispersion branches with indices $n = 1$, 2, and 3, respectively. Diagrams (c) and (d) also show the surface mode dispersion branch, labeled S. The upper and lower volume mode band frequency limits Ω_B and Ω_A, and the upper surface mode limit frequency at $\phi = 90°$, Ω_S, are shown in each diagram by the horizontal dotted lines. The surface mode aspects of Fig. 6 will be discussed shortly. The focus, for now, is on the volume mode properties.

The diagrams in Fig. 6 demonstrate the volume mode dispersion features for a YIG film and a hard [110] direction field. These features are similar to those for isotropic films. As ϕ increases from 0° to 90°, the bottom volume mode band limit frequency Ω_A moves up, the same as shown in Fig. 4. The lowest order volume mode dispersion curve has an initial slope at $kS = 0$ which is nonzero for the ϕ values below the critical angle $\phi_c = 39.3°$ and an initial slope of zero for ϕ values above ϕ_c. The key difference from the isotropic case is that, in the limit $\phi \to 90°$, the volume mode band for the anisotropic YIG film has a nonzero width. This is indicated by the surviving dispersion curves shown in diagram (d) of Fig. 6. The corresponding Fig. 5 in Ref. [1] shows a volume mode band which has collapsed to zero width in the $\phi \to 90°$ limit.

The behavior of the surface mode for YIG films is also similar to the isotropic case. Concurrent with the change in character for lowest order volume mode at $\phi = \phi_c$, a new dispersion branch emerges from the top of the volume mode band at Ω_B. In the $kS \to 0$ limit, this new surface mode reduces to the uniform mode. This new mode also has a nonzero and positive Ω vs. kS slope at $kS = 0$, and evolves with a nonreciprocal surface character with increasing kS. In effect, when ϕ exceeds ϕ_c, this surface branch becomes the characteristic mode which has a uniform profile across the film cross section in the $kS = 0$ limit. At the same time, the initial lowest order volume mode changes to a standing wave character with $k_z^{\perp} S = \pi$ and $kS = 0$. The corresponding surface mode dispersion curves are shown in diagrams (c) and (d) of Fig. 6. Working equations for the surface mode response in anisotropic films are given in the next subsection. Even though the effect of anisotropy on the overall magnetostatic mode picture for YIG materials is small, these working equations will provide an important starting point for the discussion of the surface mode for anisotropic YIG films in Section 3.2 and the considerations in Sections 4 and 5 for IRON and HEX materials.

3.2. Surface mode and surface mode suppression

As indicated in Ref. [1], the discovery of a nonreciprocal propagating mode with surface character was one of the most important results of the original analysis done by Damon and Eshbach. The surface mode can occur, in

the context of the formalism given above, if the k_z^i parameter is imaginary. The surface mode band, critical angle effects, propagation characteristics, and mode profiles were discussed in detail in Ref. [1]. The objective of this subsection is to review the basic working equations for the surface mode in the context of anisotropic films, establish some of the basic properties which will be of particular importance in the next two sections, and give some specific considerations for surface mode suppression in YIG films.

Recall that there was no a priori reason in the formalism for k_z^i to be real. Consider the effect on the scalar potential z-dependence if k_z^i is written as

$$k_z^i = i\kappa_z^i, \tag{46}$$

where κ_z^i is real. Substitution of k_z^i in this form into Eq. (22) leads to a scalar potential $Z^i(z)$ function of the form

$$Z^i(z) = a' e^{+\kappa_z^i z} + b' e^{-\kappa_z^i z}, \tag{47}$$

where the coefficients a' and b' are given in terms of the a and b coefficients as $a' = (b + ia)/2$ and $b' = (b - ia)/2$. The exponential z-dependences for the $Z^i(z)$ function in Eq. (47) lead to a mode profile with a surface character. This result was discussed in Ref. [1].

It was important in Ref. [1], and it is important here, to understand the conditions under which imaginary k_z^i and real κ_z^i solutions are possible. If k_z^i is replaced by $i\kappa_z^i$ in Eq. (33), one obtains

$$\kappa_z^i = \pm\sqrt{\frac{1 + \kappa_\alpha \sin^2\phi}{1 + \kappa_\beta}} \cdot k. \tag{48}$$

The main difference between Eqs. (48) and (33) is the absence of the negative sign *inside* the square root. In the discussions above, it was the requirement that the square root argument with a negative sign be positive that led to the $\Omega_B > \Omega > \Omega_A$ frequency condition for the volume modes. For this expression without the negative sign to be positive, the condition on frequency becomes $\Omega > \Omega_B$ or $\Omega < \Omega_A$. This means that the surface mode is possible, in principle, for all frequencies *outside* the volume mode band. As first shown by Damon and Eshbach, and discussed in Ref. [1], the frequency limits for the surface mode are much more restrictive than implied from Eq. (48) alone. For isotropic films, the surface mode is allowed for a small band of frequencies just above $\Omega = \Omega_B$. In the anisotropic film situation, similar results follow as long as the Ω_A volume mode band limit remains below the Ω_B limit. This is the situation for YIG films, and the main focus of this subsection.

The next step in the formal surface mode analysis is to rewrite Eq. (32) in terms of κ_z^i rather than k_z^i, and construct terms which apply explicitly to the applicable $\Omega < \Omega_A$ or $\Omega > \Omega_B$ range of frequencies outside the volume mode band. For the present discussion, YIG films and an Ω_A band limit which is always below the Ω_B limit are assumed. The $k_z^e = k$ condition of Eq. (34) is still applicable. One constructs appropriate counterparts to Eqs. (42) and (43) based on the $i\kappa_z^i$ replacement, Eq. (48), and the explicit expressions for κ_β and ν defined through Eqs. (10)–(16). The $k_z^e = k$ and $k_z^i = i\kappa_z^i$ replacements in Eq. (32) yield

$$k^2 + \left(k_z^i\right)^2\left(1 + \kappa_\beta\right)^2 - \nu^2 k^2 \sin^2\phi + 2k\kappa_z^i\left(1 + \kappa_\beta\right)\coth\left(\kappa_z^i S\right) = 0. \tag{49}$$

The same remarks concerning the sign of k_z^i in connection with Eq. (32) apply here to κ_z^i. Neither the z-dependence in the scalar potential, defined through the $Z^i(z)$ function in Eq. (22) and the various coefficients in Eqs. (29)–(31), nor the dispersion condition of Eq. (42), are affected by a change in sign for κ_z^i. In the surface analysis to follow, under conditions for which the square root argument in Eq. (48) is positive, κ_z^i will be taken as positive.

One then proceeds to incorporate explicit expressions for κ_β and ν defined through Eqs. (10)–(16) to obtain Eqs. (42) and (43) counterparts. The key difference from the procedure for the volume mode band is that there are now two different frequency regimes which must be considered separately, one for the above band case

$\Omega > \Omega_B$ and one for the below band case $\Omega < \Omega_A$. For both cases, the counterpart to Eq. (43) is the same and is given by

$$k = \sqrt{\frac{\Omega^2 - \Omega_B^2}{\Omega^2 - \Omega_A^2}}\,\kappa_z^i. \tag{50}$$

This is the same result as given by Eq. (46) in Ref. [1]. Here, of course, the Ω_A and Ω_B frequency parameters include the effects of anisotropy and are defined through Eqs. (13)–(16), (37) and (38).

Similar to the procedure used in Ref. [1] for the isotropic case, one may write separate counterpart equations to Eq. (42) for the above band $\Omega > \Omega_B$ and the below band $\Omega < \Omega_A$ cases. For the above band case, one obtains

$$\coth(\kappa_z^i S) = \frac{1}{2}\left[\frac{\sin^2\phi - \left[\left(\Omega^2 - \Omega_A^2\right) + \left(\Omega^2 - \Omega_B^2\right)\right]}{\sqrt{\left(\Omega^2 - \Omega_B^2\right)\left(\Omega^2 - \Omega_A^2\right)}}\right] \quad (\Omega > \Omega_B). \tag{51}$$

The counterpart equation to Eq. (51) for isotropic materials is Eq. (48) in Ref. [1]. It is to be noted that Eq. (48) in Ref. [1] has two sign errors. The sequence of signs which appear in the right-hand side square bracket numerator term should be $-$, $-$, $+$, and $-$. The corrected form of Eq. (48) from Ref. [1] and Eq. (51) above are identical in appearance. The only difference is in the new definitions for Ω_A and Ω_B through Eqs. (14)–(16), (37) and (38) to include anisotropy. Recall that $\coth(u)$ is simply $(e^u + e^{-u})/(e^u - e^{-u})$. From this definition, and with κ_z^i taken as positive, the left-hand side of Eq. (51) is always positive. This means that above band $\Omega > \Omega_B$ solutions to Eq. (51) are possible only for the range of propagation angle ϕ for which the numerator of the right-hand side square bracket term is also positive. The resulting range of propagation angles for the above band surface mode is given by $\phi > \phi_c$, where ϕ_c is the same critical angle specified by Eq. (45).

Subject to the $\phi > \phi_c$ condition, one may obtain equations which define the surface mode band above $\Omega = \Omega_B$ from the same approach discussed in Section 5 of Ref. [1]. For a given ϕ value, Eq. (51) yields one dispersion branch which ranges from $\kappa_z^i S = 0$ and $\Omega = \Omega_B$ at $kS = 0$ to $\kappa_z^i S = \infty$ and $\Omega = \Omega_U$ at $kS = \infty$. For a given propagation angle ϕ, the limiting frequency at the top of the surface mode band, Ω_U, is given by

$$\Omega_U = \sqrt{\Omega_B^2 + \frac{\left(\Omega_\alpha + 1\right)^2\left(\sin^2\phi - \sin^2\phi_c\right)^2}{4\sin^2\phi}} \quad (\phi > \phi_c). \tag{52}$$

Eq. (52) specifically demonstrates the collapse of the top of the surface mode band to Ω_B in the limit $\phi \to \phi_c$. In the isotropic limit, Ω_α and Ω_β both reduce to Ω_H and Eq. (52) reduces to Eq. (49) in Ref. [1]. The curve labeled Ω_U in Fig. 4 represents a plot of Eq. (52). The region between Ω_U and Ω_B represents the surface mode band. This is the counterpart to the cross hatched 'SURFACE' region in Fig. 2 of [1]. Note: the curve labeled Ω_S in Fig. 2 of Ref. [1] actually corresponds to the Ω_U parameter from Eq. (49) of Ref. [1].

Diagrams (c) and (d) of Fig. 6, discussed above, also show the above band surface mode dispersion curves for the two propagation angles which are above the critical angle ϕ_c. The top limit frequencies for these dispersion curves corresponds to Ω_U. The upper horizontal dashed line in the diagrams represents the top limit surface mode frequency at $\phi = 90°$, Ω_S.

Return now to consider possible surface modes below band, subject to the $\Omega < \Omega_A$ condition. Recall that for the present YIG case, $\Omega_A < \Omega_B$ is also satisfied so that Ω satisfies $\Omega < \Omega_B$ as well. In this below band regime, Eqs. (49) and (50) combine to yield a surface mode counterpart to Eq. (42) of the form

$$\coth(\kappa_z^i S) = -\frac{1}{2}\left[\frac{\sin^2\phi + \left(\Omega_B^2 - \Omega^2\right) + \left(\Omega_A^2 - \Omega^2\right)}{\sqrt{\left(\Omega_B^2 - \Omega^2\right)\left(\Omega_A^2 - \Omega^2\right)}}\right] \quad (\Omega < \Omega_A). \tag{53}$$

Given the positive definite property of the left-hand side of Eq. (53), it is evident that there are no below band surface modes. Eq. (53) is identical in form to Eq. (47) in Ref. [1] and the YIG below band situation is similar to the isotropic case. The surface mode, if present, will appear above the volume mode frequency band only and satisfy the dispersion relation implicit in Eqs. (50) and (51). In contrast with the volume mode dispersion condition which involves $\cot(k_z^{\perp} S)$ and multiple branches, the $\coth(\kappa_z^{\perp} S)$ function in Eq. (51) has only a single branch. It is only necessary to consider the limitations imposed by the right-hand side function, in combination with Eq. (50), to determine the surface mode dispersion characteristics. As discussed in Ref. [1], the surface mode has a number of peculiar properties. These include frequencies which are generally above the top of the usual spin wave band at low wave numbers and a nonreciprocal surface character. These properties were discussed in detail in Ref. [1] and the basic conclusions there also apply to YIG materials.

It is important to emphasize the conditions under which the above analysis applies, namely, the YIG materials situation for which the stiffness frequencies Ω_α and Ω_β satisfy the condition $\Omega_\alpha + 1 > \Omega_\beta > \Omega_\alpha$. The $\Omega_\beta > \Omega_\alpha$ condition ensures that the volume band limit frequencies Ω_A and Ω_B always satisfy the $\Omega_A < \Omega_B$ condition and that band inversion does not occur. The $\Omega_\alpha + 1 > \Omega_\beta$ condition ensures the existence of a critical angle ϕ_c, along with the changes in character for the lowest order volume mode and the appearance of a surface mode branch as ϕ moves from below to above ϕ_c.

If, however, Ω_β could be made sufficiently large relative to Ω_α, the $\Omega_\beta > \Omega_\alpha$ condition for a non-inverted volume mode band of the sort shown in Fig. 4 would be satisfied but the $\Omega_\alpha + 1 > \Omega_\beta$ condition for ϕ_c would not be satisfied. Under these conditions, one would still have a volume mode band as shown in Fig. 4, but the families of volume mode dispersion curves would all have the character shown by the family of V curves in diagrams (a) and (b) of Fig. 6 and the surface mode band and dispersion curves would be completely suppressed.

The above scenario can be realized for YIG materials by simply increasing the magnitude of the anisotropy field while decreasing the saturation induction $4\pi M_s$. For example, in YIG materials magnetized to saturation along the in-plane [110], $\Phi = 45°$ direction by an applied in-plane field H_o which is greater than $|H_A|$, the requirement for surface mode suppression, $\Omega_\beta > \Omega_\alpha + 1$, may be evaluated from Eqs. (14)–(16) as $\frac{3}{2}|H_A| > 4\pi M_s$. The $\frac{3}{2}$ factor comes from the combination of anisotropy field terms in $H_\alpha - H_\beta$. One well known way to decrease $4\pi M_s$ and increase $|H_A|$ in YIG materials is by appropriate substitutions of calcium and vanadium in the $Y_3Fe_5O_{12}$ yttrium iron garnet composition [58,59]. A substituted '400 GAUSS' material with $4\pi M_s = 400$ G and $H_A = -300$ Oe, for example, would result in a volume mode band similar to that shown in Fig. 4 but shifted up in reduced frequency, and no surface mode at all.

4. Results for IRON films

The discussion of YIG materials in the previous section presented representative results for materials and field configurations which satisfy the $\Omega_\beta > \Omega_\alpha$ stiffness frequency condition. This results in a non-inverted volume mode band with $\Omega_B > \Omega > \Omega_A$ over the entire range of in-plane propagation angles, $0° < \phi < 90°$. Under conditions for which the opposite condition is true, namely $\Omega_\alpha > \Omega_\beta$, both the volume and the surface mode dispersion curves take on new properties not yet considered.

As one example of a situation for which this condition is realized in real materials, this section will consider IRON films or slabs with parameters as listed in column 3 of Table 1. The key change from the YIG materials of Section 3 is that the first order cubic anisotropy constant K_1 is now positive. The parameters in column 3 of Table 1 are typical of pure iron, with a saturation induction $4\pi M_s$ of 21 kG and a positive first order cubic anisotropy field H_A of + 600 Oe. As evident from Eqs. (15) and (16), these values result in H_α and H_β stiffness fields which (1) decrease rather than increase as the field orientation angle Φ is increased from zero and (2) give H_α values which are greater than the corresponding H_β values.

The actual variations in H_α and H_β with Θ for the IRON parameters listed in Table 1 are shown in Fig. 7.

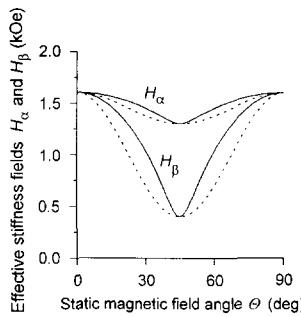

Fig. 7. Variation of the two effective stiffness fields H_α and H_β with the angle Θ between the in-plane cubic [100] direction and the direction of a 1000 Oe in-plane static magnetic field for an IRON film with a first order magnetocrystalline anisotropy field H_A of +600 Oe. The solid lines show the variation in the H_α and H_β with Θ without the quasi-lineup approximation. That is, the magnetization angle Φ relative to the in-plane [100] direction is determined through the static equilibrium condition. The dashed lines show the variation in H_α and H_β with Θ under the quasi-lineup approximation $\Phi = \Theta$.

The format for Fig. 7 is the same as for Fig. 3. Because of the small static external field value of 1000 Oe, relative to the large value of H_A at 600 Oe, the quasi-lineup assumption is not particularly well satisfied except near 0°, 45°, and 90°. The field is sufficient to saturate the magnetization vector parallel to the field direction at $\Theta = \Phi = 45°$. The relative change in the stiffness fields as Θ varies from zero and 45° is quite large. The out-of-plane stiffness field H_α varies from 1600 Oe at $\Theta = 0°$ down to 1300 Oe at $\Theta = 45°$, nearly a 20% decrease. The in-plane stiffness field H_β varies from 1600 Oe at $\Theta = 0°$ down to 400 Oe at $\Theta = 45°$, for a 75% decrease. Note that for positive anisotropy materials, the $\Phi = 0°$ or [100] direction is an easy direction. In the hard [110] or $\Theta = \Phi = 45°$ direction, the H_α stiffness field of 1300 Oe is significantly greater than the H_β stiffness field of 400 Oe.

The reordering of these stiffness fields and, hence, the stiffness frequencies Ω_β and Ω_α as well, leads to the volume mode band inversion at the second critical angle ϕ_x, defined as the propagation angle at which the Ω_B and Ω_A band limit frequencies cross. This angle, introduced in Section 3, is given by

$$\phi_x = \sin^{-1}\sqrt{\frac{\Omega_\beta}{\Omega_\alpha}}\,. \tag{54}$$

Note that this band inversion or $\Omega_B - \Omega_A$ crossover angle is defined only when the $\Omega_\alpha > \Omega_\beta$ condition is satisfied. For the IRON parameters in Table 1, the surface mode critical angle ϕ_c is 7.7° and the volume mode band crossover angle ϕ_x is 33.7°.

4.1. Band inversion and forward volume waves

Fig. 8 shows the two volume mode band frequency limits Ω_A and Ω_B and the volume mode band as a function of the propagation angle ϕ for the IRON parameters and the $\Theta = 45°$ hard direction 1000 Oe field situation indicated above. It also shows the ϕ-dependent surface mode band limit frequency Ω_U which emerges from the top of the volume mode band at $\phi = \phi_c \approx 7.7°$. The format is the same as in Fig. 4. The regions between the Ω_A and Ω_B curves are labeled V to indicate the volume mode band. The region between Ω_U and Ω_B for propagation angles between ϕ_c and $\phi_x \approx 33.7°$, and between Ω_U and Ω_A for angles between ϕ_x and 90°, is labeled S to indicate the surface mode band. The left-side vertical scale gives the reduced frequencies and the right-side vertical scale gives actual frequencies in GHz. These frequencies extend to significantly higher frequencies than is the case for the YIG materials and the bands tend to be wider because of the large saturation induction for iron. Note that the static applied field is the same as in the YIG case.

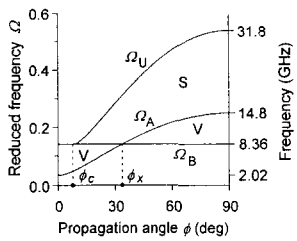

Fig. 8. Theoretical volume and surface mode bands as a function of in-plane propagation angle ϕ for a (100) plane IRON film with cubic magnetocrystalline anisotropy. The Ω_A and Ω_B curves show the limits for the volume mode band and the crossover effect at $\phi_x \approx 33.7°$. The curve labeled Ω_U shows the top of the surface mode band which emerges from the top of the volume mode band at a critical propagation angle $\phi_c \approx 7.7°$. The V and S labels designate the volume and surface mode bands, respectively. The curves are based on values for the static in-plane field H_0, the film saturation induction $4\pi M_s$, a cubic anisotropy field H_A, and a field angle Θ relative to the [100] cubic axis of 1000 Oe, 21 kG, +600 Oe, and 45°, respectively. The scale on the right-side vertical axis gives limit frequency values in GHz.

The volume mode band in Fig. 8 has a very different character from either the volume mode band for YIG materials shown in Fig. 4 or the volume mode band shown in Fig. 2 of Ref. [1] for isotropic films. The Ω_B band limit is independent of propagation angle, as before. The Ω_A band limit starts out well below Ω_B for $\phi = 0$ and curves upward, also as before. For this IRON case, however, Ω_A continues to increase, moves above Ω_B at the crossover angle ϕ_x, and then produces an inverted volume mode band for propagation angles above ϕ_x.

Volume mode inversion simply means that the usual bottom and top band limits Ω_A and Ω_B in the DE theory are reversed and the band is essentially flipped over. This is evident from the two V labels in Fig. 8 for $\phi < \phi_x$ and $\phi > \phi_x$. One consequence of this inversion is also a flip in the character of the dispersion curves within the band, to be discussed shortly.

As before, it is important to realize that each propagation angle value in Fig. 8 corresponds to an infinite manifold of volume mode dispersion curves of frequency vs. wave number, all contained between the Ω_A and Ω_B frequency limits indicated. Each angle also corresponds to a single surface mode dispersion curve between the appropriate Ω_A or Ω_B lower frequency limit and the upper frequency limit for the surface mode, Ω_U.

As long as the propagation angle is below the crossover angle ϕ_x, all of the discussion of the previous section regarding the volume mode dispersion solutions and profiles applies. This includes the solution details based on Eqs. (42) and (43) and Fig. 5, and the basic dispersion curve results shown by the dispersion diagrams in Fig. 6. When the volume mode band inverts, however, the situation changes in several important ways. In order to understand these changes, it is necessary to consider the counterparts to Eqs. (42) and (43) when the frequency condition $\Omega_A > \Omega > \Omega_B$ is satisfied. Following the same type of manipulations of Eqs. (35) and (36) which led to Eqs. (42) and (43) for the volume modes in YIG films, one can obtain characteristic working equations for the inverted band situation given by

$$\cot\left(k_z^i S\right) = H_a(\Omega) = \frac{1}{2}\left[\frac{\left(\Omega_A^2 - \Omega^2\right) + \sin^2\phi - \left(\Omega^2 - \Omega_B^2\right)}{\sqrt{\left(\Omega_A^2 - \Omega^2\right)\left(\Omega^2 - \Omega_B^2\right)}}\right], \tag{55}$$

and

$$k = \sqrt{\frac{\Omega^2 - \Omega_B^2}{\Omega_A^2 - \Omega^2}}\, k_z^i. \tag{56}$$

The solutions for k_z^i versus Ω for the various dispersion branches follow from the intersection between the $H_a(\Omega)$ function and the corresponding $n = 1$, $n = 2$, $n = 3$, etc., branches of the $\cot(k_z^i S)$ function indicated in

Fig. 5, similar to the procedure before but with the $G_a(\Omega)$ function of Eq. (42) replaced by the $H_a(\Omega)$ function of Eq. (55). The corresponding value of the propagation wave number k is then obtained from Eq. (56).

Consider first the properties of the solutions in the $\Omega \to \Omega_B$ frequency limit, at what has now become the bottom frequency limit for the inverted volume mode band. In this limit, $H_a(\Omega)$ diverges to $+\infty$ and the corresponding solutions for $k_z^i S$ are 0, π, 2π,.... From Eq. (56) the corresponding value of k in the $\Omega \to \Omega_B$ limit for all of the volume mode branches is zero. One has, in this lower band edge limit for the inverted band, a similar situation to the upper band edge limit for the non-inverted volume mode band case. The modes are all nonpropagating modes at $k = 0$, but with characteristic profiles across the film cross section which correspond to a uniform mode with $k_z^i S = 0$ for the first branch, and standing modes with wavelengths of $2S$, S, $2S/3$,..., for the higher order branches. The actual dynamic magnetization profiles in this limit correspond to the uniform mode and quasi-unpinned standing wave modes, as discussed in detail in Ref. [1].

Now consider the properties of the inverted band volume mode solutions in the $\Omega \to \Omega_A$ frequency limit, at what has now become the top frequency limit for the band. In this limit, the sign of the divergence for $H_a(\Omega)$ depends on the sign of the numerator quantity $H_{top} = [\sin^2\phi - (\Omega_A^2 - \Omega_B^2)]$. From the definitions of Ω_A and Ω_B through Eqs. (37) and (38), one can see that H_{top} will be positive for all propagation angles $\phi_x < \phi < 90°$ if the condition $\Omega_\beta + 1 > \Omega_\alpha$ is satisfied. For the IRON configuration, this reduces to the anisotropy condition $\frac{3}{2}H_A < 4\pi M_s$, with H_A positive. The iron parameters in Table 1 satisfy this condition. Similar to the YIG case, the $\frac{3}{2}$ factor comes from the combination of anisotropy field terms in $H_\alpha - H_\beta$. From Fig. 5, the corresponding solutions for $k_z^i S$ in this top-of-the-band $\Omega \to \Omega_A$ limit are now 0, π, 2π,..., the same as the bottom-of-the-band $\Omega \to \Omega_B$ values.

Now consider the limiting values of the propagation wave number k at the band limits. At the bottom-of-the-band $\Omega \to \Omega_B$ limit, it is clear from Eq. (56) that one has $k \to 0$ for all branches. In order to obtain the corresponding k values in the top-of-the-band $\Omega \to \Omega_A$ limit, it is first necessary to have an expression for $k_z^i S$ in this limit. From Eq. (55), one obtains the value of $k_z^i S$ for the nth $\cot(k_z^i S)$ branch curve in Fig. 5 in the $\Omega \to \Omega_A$ limit as

$$\left[k_z^i S\right]^{(n)} = \frac{2\sqrt{\left(\Omega_\alpha \sin^2\phi - \Omega_\beta\right)\left(\Omega_A^2 - \Omega^2\right)}}{\Omega_\beta - (\Omega_\alpha - 1)\sin^2\phi} + (n-1)\pi. \tag{57}$$

Eq. (57), in combination with Eq. (56), gives $k \to \infty$ for all branches except for the lowest order $n = 1$ branch. For the $n = 1$ branch, the identical $(\Omega_A^2 - \Omega^2)^{1/2}$ terms in the denominator of Eq. (56) and the numerator in Eq. (57) cancel to give a finite value for k at the top of the inverted volume mode band. The top-of-the-band k value for the $n = 1$ volume mode dispersion branch is given by

$$k^{(1)} = \frac{1}{S}\frac{2\left(\Omega_\alpha \sin^2\phi - \Omega_\beta\right)}{\Omega_\beta - (\Omega_\alpha - 1)\sin^2\phi}. \tag{58}$$

The results given above indicate a volume mode situation for the inverted volume mode band in IRON materials which is very different from the case for the non-inverted band. First of all, the band of dispersion curves is flipped over. All dispersion curves start out at the bottom of the band at $\Omega = \Omega_B$ and $k = 0$, and the branch frequencies increase with increasing wave number. The slopes of these dispersion curves are all positive and correspond to forward volume modes rather than backward volume modes. Forward volume modes are typically encountered in films which are magnetized perpendicular to the film plane [60]. Because of the positive anisotropy, it is possible to obtain forward volume modes for in-plane magnetized films.

Second, the mode profiles have the same $k_z^i S$ values of 0, π, 2π,..., for frequencies at both of the band limits. This means that the lowest order dispersion branch starts out at $\Omega = \Omega_B$, $k_z^i S = 0$, and $k = 0$ and ends at $\Omega = \Omega_A$, $k_z^i S = 0$, and $k = k^{(1)}$. The $k_z^i S = 0$ property in combination with a nonzero k value at $\Omega = \Omega_A$ for this $n = 1$ mode corresponds to a propagating uniform mode of sorts. The mode represents a propagating wave,

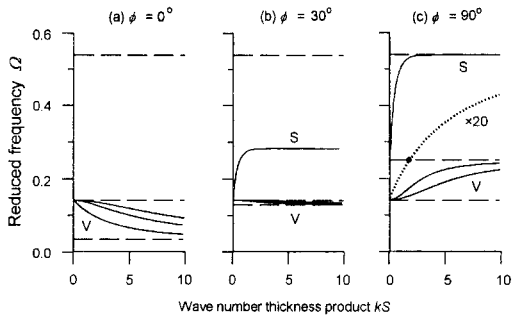

Fig. 9. Dispersion curves of reduced frequency Ω vs. reduced wave number kS for three values of the propagation angle ϕ, as indicated. The solid curves in each diagram labeled V correspond to the three lowest order volume mode dispersion branches. The solid curve labeled S in diagrams (b) and (c) for $\phi > \phi_c = 7.7°$ shows the surface mode dispersion curve. The dotted curve in diagram (c) shows the common lowest order V curve and the S curve on an expanded horizontal scale by a factor of 20. The solid dot in diagram (c) indicates the point of volume to surface mode conversion for the dotted line dispersion branch. The volume mode band limit frequencies Ω_B and Ω_A, and the $\phi = 90°$ surface mode band limit frequency Ω_S, are shown in each diagram by the horizontal dashed lines. All curves are for an IRON film and are based on values for the static in-plane field H_0, the film saturation induction $4\pi M_s$, a cubic anisotropy field H_A, and a field angle Θ relative to the [100] cubic axis of 1000 Oe, 21 kG, +600 Oe, and 45°, respectively, as for Fig. 8.

but the wave front through the film is uniform. The higher order modes, on the other hand, start out and end with the same standing wave wavelengths of $2S$, S, $2S/3, \ldots$, across the film at $\Omega = \Omega_B$ and $k = 0$ and at $\Omega = \Omega_A$ and $k = \infty$. The dynamic magnetization profiles are different, however, in that the profiles are quasi-unpinned in the $\Omega = \Omega_B$ and $k = 0$ limit and quasi-pinned in the $\Omega = \Omega_A$ and $k = \infty$ limit, similar to the situation for YIG and isotropic films [1].

The third point of difference is in the truncated wave number character for the lowest order volume mode dispersion branch and the finite value of $k^{(1)}$ at the top of the band. For the IRON case parameters in Table 1, $k^{(1)}S$ is numerically equal to 0.1. For iron films in the 100–1000 Å thickness range, this $k^{(1)}S$ corresponds to k values in the 10^4–10^5 cm^{-1} range, roughly at the high end of the usual MSW range and in the range usually accessible by Brillouin light scattering experiments [50]. This truncation goes hand in hand with the propagating uniform profile property noted above. As will be evident from the discussion below, this uniform profile truncated k-mode connects smoothly with the surface mode for frequencies above Ω_A.

Fig. 9 shows actual dispersion curves calculated for the IRON case. The format for Fig. 9 is the same as for Fig. 6. The figure shows a series of dispersion curve diagrams for three values of the propagation angle ϕ, at $\phi = 0°$, 30°, and 90°, and the same parameters used for Fig. 8. The $\phi = 0°$ case in diagram (a) corresponds to $\phi < \phi_c = 7.7°$ and no surface mode. The $\phi = 30°$ case of diagram (b) corresponds to $\phi_c < \phi < \phi_x = 36.7°$ with a surface mode but no crossover. The volume mode band is relatively narrow at this ϕ value. The $\phi = 90°$ case in diagram (c) corresponds to $\phi > \phi_x$ with a surface mode in combination with volume mode crossover and band inversion. As for the band limit curves in Fig. 8, the dispersion curves in Fig. 9 are of reduced frequency Ω vs. reduced wave number kS. The horizontal dashed lines indicate the relevant ϕ-dependent Ω_A band edge, the ϕ-independent band edge Ω_B, and the Ω_S surface mode band edge at $\phi = 90°$.

Each diagram shows the three lowest order volume mode dispersion curves, indicated by the common label V. Diagrams (b) and (c) also show the surface mode dispersion branch, labeled S. The lowest order branch in diagram (c), for $\phi = 90°$, is also shown on an expanded $\times 20$ kS scale as a dotted line. This branch passes through the top of the volume mode band at Ω_A and approaches the limiting frequency at the top of the surface mode band, Ω_S in this case, in the limit $k \to \infty$. This 'pass through' point at $\Omega = \Omega_A$ is indicated by a solid dot.

Diagrams (a) and (b) in Fig. 9 show the same dispersion features which are found in the YIG situation considered in Section 3. Diagram (a), for $\phi = 0°$, corresponds to the basic backward volume mode situation,

with no surface mode, in diagram (a) of Fig. 6. Diagram (b), for $\phi = 30°$, corresponds to a propagation angle just below the crossover point but well above the critical angle ϕ_c. In this situation, the width of the volume mode band is quite small and the surface dispersion branch is well developed. The basic properties of these modes follow the discussion given above for YIG materials and in Ref. [1] for isotropic materials.

Turn now to diagram (c) in Fig. 9, for $\phi = 90°$. Keep in mind that for this propagation direction, as for all angles above the crossover angle ϕ_x, the volume mode band is now inverted. These curves are quite different from the previous cases. First, all of the volume mode dispersion curves now increase in frequency from Ω_B as k increases from zero. The positive slope for these curves corresponds to a forward volume mode character in place of the previous backward volume mode character. Second, the lowest order dispersion branch is highly localized near $k = 0$ and truncates at a very low value of kS in the limit $\Omega \to \Omega_A$ at the now inverted top of the volume mode band. This lowest order volume mode dispersion branch is barely discernable next to the vertical axis in the diagram. The dotted line shows this lowest order dispersion branch expanded out in k by a factor of 20. From this expanded curve, the kS value for this branch at the top of the volume mode band at Ω_A is only 0.1 or so. The branch is shown to extend to frequencies above Ω_A. The branch segment above Ω_A has a surface mode character. The properties of this segment and the nature of the conversion between volume- and surface-like properties is considered below.

4.2. Re-entrant volume modes and surface mode

The operational equations for the treatment of the surface mode in the $\phi > \phi_x$ range of propagation angles are Eqs. (50) and (51), as in Section 3.2. The important difference here is in the range of applicable frequencies. For the YIG configuration, the range of surface mode frequencies was $\Omega_B > \Omega > \Omega_U$. For the IRON configuration, the range of surface mode frequencies is also $\Omega_B > \Omega > \Omega_U$ for propagation angles below ϕ_x, but is $\Omega_A > \Omega > \Omega_U$ for angles above ϕ_x. Just as volume mode band inversion and the interchange of the Ω_A and Ω_B band limits leads to the $k_z^i \to 0$ and $k \to k^{(1)}$ truncation effect for the lowest order volume mode dispersion branch at the top of the volume mode band in the $\Omega \to \Omega_A$ limit, the replacement of Ω_B by Ω_A as the lower band limit for the surface mode in the $\phi > \phi_x$ regime of propagation angles also leads to a truncation effect.

Considered in the $\Omega \to \Omega_A$ limit approached from frequencies above Ω_A, Eqs. (50) and (51) lead immediately to limiting values for $\kappa_z^i \to 0$ and for $k \to k^{(1)}$. The large solid dot on the expanded scale lowest order dispersion curve in the right most diagram of Fig. 9 represents this $k^{(1)}$ wave number position. Now, however, the surface mode begins at $\kappa_z^i = 0$ and a nonzero value of the propagating wave number, and not as the uniform mode at $\kappa_z^i = 0$ and $k = 0$ which characterized isotropic and YIG materials.

The above result indicates that there are actually two frequency points at which the dynamic response across the film cross section is uniform, one at the bottom of the volume mode band at $\Omega = \Omega_B$ and one at the boundary between the volume mode band and the surface mode band at $\Omega = \Omega_A$. The first frequency point corresponds to $k_z^i = 0$ and $k = 0$. The second frequency point corresponds to $k_z^i = \kappa_z^i = 0$ and $k = k^{(1)}$. This behavior represents a re-entrant character, in which k_z^i starts out at zero in the uniform mode limit at the bottom of the volume mode band, increases from this zero value as the frequency is increased, and then returns to zero again at the top of the volume mode band. During this re-entrant behavior, the value of the propagating wave number k simply increases from zero to $k^{(1)}$. As one then passes through to the surface mode band, k_z^i is replaced by κ_z^i. This κ_z^i parameter starts out at $\kappa_z^i = 0$ for $k = k^{(1)}$ at the top of the volume mode band and the bottom of the surface mode band, and then increases as the frequency is increased. For frequencies approaching the top of the surface mode band at Ω_U, k and κ_z^i become very large and approximately equal. In the $\Omega \to \Omega_U$ limit, k and κ_z^i diverge.

The re-entrant behavior for k_z^i and κ_z^i at $\phi = 90°$ is shown in Fig. 10. The curves are based on the same IRON situation used for the previous results of this section. The graph shows the variations in the volume mode $k_z^i S$ parameter and the surface mode $\kappa_z^i S$ parameter with frequency over their applicable frequency regimes,

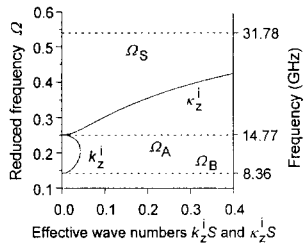

Fig. 10. Diagram showing the variation in the effective wave number or decay component in the direction normal to the film, k_z^i or κ_z^i, multiplied by the film thickness S, as a function of reduced frequency across the applicable volume mode or surface mode band for $\phi = 90°$, with frequency shown on the vertical axis. The volume mode band limit frequencies Ω_B and Ω_A and the surface mode band limit frequency Ω_S are shown by the horizontal dashed lines. The curves are for an IRON film and are based on values for the static in-plane field H_0, the film saturation induction $4\pi M_s$, a cubic anisotropy field H_A, and a field angle Θ relative to the [100] cubic axis of 1000 Oe, 21 kG, +600 Oe, and 45°, respectively, as for Figs. 8 and 9.

$\Omega_B > \Omega > \Omega_A$ for $k_z^i S$ and $\Omega_A > \Omega > \Omega_U$ for $\kappa_z^i S$. As with previous band and dispersion graphs, frequency is shown on the vertical axis and the wave number related parameters are shown on the horizontal axis. In this case, the horizontal axis gives the $k_z^i S$ and $\kappa_z^i S$ values which go with the volume mode region or the surface mode region, respectively. The horizontal dashed lines labeled Ω_B and Ω_A delineate these regions. The curve for $\Omega_B < \Omega < \Omega_A$ shows $k_z^i S$ versus Ω; the upper curve for $\Omega > \Omega_A$ shows $\kappa_z^i S$ versus Ω.

The key result in Fig. 10 is the re-entrant nature of $k_z^i S$ as the frequency Ω moves from the bottom of the volume mode band at $\Omega = \Omega_B$ to the top of the band at $\Omega = \Omega_A$. The $k_z^i S = 0$ result at both band edges corresponds to a uniform dynamic magnetization profile across the film at both band edges as well. Such a uniform profile at the bottom band edge, Ω_B, occurs at the point for which one also has $k = 0$. This corresponds to the uniform mode response discussed above and at length in Ref. [1]. A uniform profile at the top band edge, Ω_A, is different. Here, one has a nonzero value of the wave number k. This mode at the top of the band, therefore, corresponds to a propagating plane-wave like mode with a uniform dynamic response across the film.

Note further, that the maximum value of $k_z^i S$ in the middle of the volume mode band is not large. This maximum value for the IRON situation shown in Fig. 10 is around 0.04. This small $k_z^i S$ maximum corresponds to a large wavelength which is more than 150 times the film thickness. From a practical point of view, therefore, the 're-entrant' $k_z^i S$ character for the lowest order volume mode really amounts to a mode which is more-or-less uniform across the film cross section for the entire width of the volume mode band. As soon as the frequency moves into the surface mode regime above Ω_A, the profile across the film cross section takes on the decay-like character specified in terms of $\kappa_z^i S$. Fig. 10 shows that, as soon as one is in this region, $\kappa_z^i S$ increases rapidly as Ω is increased further and the mode profile quickly takes on the expected highly localized surface mode character already considered.

As indicated in the Introduction, re-entrant surface mode and band inversion effects have also been predicted for multilayers [40–42]. In these works, however, these effects were rather imbedded in a formal theory and implicit in the various band diagrams. The explicit effects discussed above were not explored in detail.

5. Results for HEX films

This closing section considers situations under which the third critical angle ϕ_p can be realized. Such a situation can occur for cubic materials with a large positive H_A which is greater than $\frac{2}{3}4\pi M_s$, when the film is magnetized to saturation along an in-plane [110] direction. These conditions satisfy the $\Omega_\alpha > \Omega_\beta + 1$ requirement for the third critical angle, $\phi_p = \sin^{-1}[\Omega_\beta/(\Omega_\alpha - 1)]^{1/2}$. The situation described above for IRON materials and $\phi > \phi_x$, with truncated k values, re-entrant properties for the lowest order volume mode, and a

surface mode which picks up at this truncated k value at the top of the volume mode band, will only occur up to this third critical angle, or for $\phi_x < \phi < \phi_p$. Above this third critical angle, the numerator term in Eq. (55) will be negative rather than positive in the $\Omega \to \Omega_A$ limit at the top of the volume mode band. From Eq. (55), then, the lowest order volume mode $k_z^1 S$ value in the $\Omega \to \Omega_A$ limit will now be π rather than zero. This result, in combination with Eq. (56), leads to a corresponding value of the wave number k at the top of the volume mode band which no longer truncates but diverges to infinity in the $\Omega \to \Omega_A$ limit. For $\phi_x < \phi < \phi_p$, therefore, the volume mode band becomes a 'flipped over' version of the volume mode band for $\phi < \phi_c$.

At the same time, the negative divergence in combination with Eq. (51) leads to the elimination of surface mode solutions. The practical effect is that the top of the surface mode band, specified through Eq. (53) and Ω_U, merges with the top of the volume mode band at Ω_A as the propagation angle ϕ approaches ϕ_p.

The above effects may be realized in real materials, namely, barium ferrite slabs or films with uniaxial anisotropy and an in-plane easy axis. Typical parameters for such a film are listed in column 4 of Table 1. Note that the uniaxial anisotropy invokes different terms in the H_α and H_β stiffness field expressions of Eqs. (15) and (16), but the net effect is the same. The parameters in Table 1 yield reduced stiffness frequency values $\Omega_\alpha = 4.26$ and $\Omega_\beta = 0.85$. These satisfy the $\Omega_\alpha > \Omega_\beta + 1$ condition for a ϕ_p critical angle and the surface band merge effect described above.

Fig. 11 shows volume and surface mode band limit diagrams for the HEX case. The format of the diagrams in Fig. 11 is the same as that for the band diagrams in Figs. 4 and 8. The left-side vertical scale gives the reduced frequencies and the right-side vertical scale gives actual frequencies in GHz. The curves which correspond to the Ω_A, Ω_B and Ω_U frequencies are labeled as such. The bottom diagram shows plots of the two volume mode band frequency limits Ω_A and Ω_B and the corresponding volume mode band as a function of the propagation angle ϕ for the HEX parameters and the $\Theta = 90°$ hard direction 20 kOe field situation listed in column 4 of Table 1. Barely discernable near the crossover point is the surface mode band edge limit curve which corresponds to Ω_U. The upper diagram shows the surface mode band limit curve on a more expanded scale.

In some respects, the band diagram in Fig. 11 is similar to the diagram for the IRON case, with the volume mode band inversion at a crossover critical angle at $\phi_x = 26.6°$. The main difference, on the scale of the bottom diagram, is in the absence of a pronounced surface mode band. A surface mode band is present, but is severely

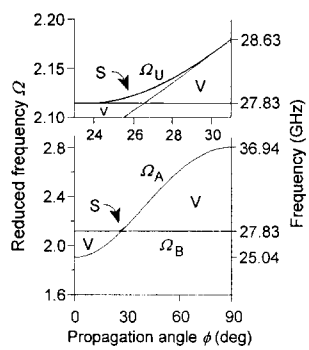

Fig. 11. Theoretical volume mode and surface mode band edge frequencies Ω_A, Ω_B, and Ω_U as a function of in-plane propagation angle ϕ for a HEX film with uniaxial magnetocrystalline anisotropy and an in-plane easy axis at 90° to the in-plane static field and saturation magnetization direction. The lower diagram shows the entire band; the Ω_A and Ω_B curves define the volume mode band edges. The V labels designate the volume mode band. The surface mode band edge curve, labeled S and barely discernable in the lower diagram, is shown on an expanded scale in the upper diagram. The heavy line in the top diagram, indicated by S and labeled Ω_U, shows the top of the surface mode band. The curves are based on values for the static in-plane field H_0, the film saturation induction $4\pi M_s$, a cubic anisotropy field H_A, and a field angle Θ relative to the uniaxial axis of 20 kOe, 4.7 kG, 16 kOe, and 90°, respectively. The scale on the right-side vertical axis gives limit frequency values in GHz.

limited both in frequency and range of propagation angles. Note from Table 1 that this HEX case corresponds to critical angles $\phi_c = 23.7°$ and $\phi_p = 30.8°$. The surface mode band is shown with better resolution in the expanded diagram at the top of Fig. 11. The band, albeit quite limited in size, has a much different character from the previous cases. In this HEX situation, the surface mode band appears to exit smoothly from the volume mode band at $\phi = \phi_c$ and smoothly merge back into the inverted volume mode band at $\phi = \phi_p$. In the range of propagation angles between ϕ_c and ϕ_x, the surface mode and the volume mode dispersion curves have the characteristics described in Section 3 for YIG materials, except that the width of the surface band is very small. Similarly, for the range of propagation angles between ϕ_x and ϕ_p, the truncation effects of Sections 4 are obtained. For propagation angles above ϕ_p, the surface mode band edge has merged back into the inverted volume mode band.

6. Summary

A modified formulation of the Damon–Eshbach theory of magnetostatic waves for in-plane magnetized anisotropic films has been developed. The formal development incorporates two effective magnetic field parameters rather than the single field in the DE theory. Several distinct types of anisotropy were investigated in terms of real material parameters corresponding to YIG, iron, and hexagonal ferrite materials. It is found that the different anisotropies had significant effects on both the volume and surface magnetostatic modes.

In materials similar to YIG, the presence of anisotropy can suppress the DE surface mode entirely. For the iron and hexagonal ferrite materials, both the DE surface and volume modes are drastically influenced by the anisotropy. In particular, two new critical in-plane propagation angles are found. The first critical angle marked the inversion from a BVW band to a FVW band of excitations. The second critical angle is associated with a merging of the surface mode back into the volume mode band. The presence of a re-entrant MSW dispersion branch was also demonstrated. This leads to a uniform mode excitation at two distinct frequencies. The lower frequency corresponds to FMR. The higher frequency corresponds to a propagating mode with a uniform dynamic response across the film thickness.

Acknowledgements

This work was started while one of the authors (CEP) was on sabbatical in 1984/1985 and supported in part by the Department of Physics, Simon Fraser University, Burnaby, BC, Canada. The authors gratefully acknowledge Drs. J.F. Cochran of Simon Fraser University, R.L. Stamps of Ohio State University, Lima campus, R.E. Camley of the University of Colorado at Colorado Springs, and B. Hillebrands of the Universität Kaiserlautern, Germany for helpful discussions. The work was supported in part by the National Science Foundation, grant Nos. DMR-8921761 and DMR-9400276, the U.S. Army Research Office, grant Nos. DAAL03-91-G-0327 and DAAH04-95-1-0325, and the Office of Naval Research, grant Nos. N00014-90-J-4078 and N00014-94-1-0096.

Appendix A. Effective fields for anisotropic films

A useful starting point to obtain the effective field equations provided in Section 2 is the expression for the free energy of the magnetic system written in terms of the components of the total internal magnetic field $\boldsymbol{H}$ and the general magnetization vector $\boldsymbol{M}$ in the X–Y–Z sample reference frame in Fig. 1. For the purposes of this analysis, three energy contributions are considered. The Zeeman energy, or field energy, is given as

$$F_H = -\boldsymbol{M} \cdot (\boldsymbol{H}_o + \boldsymbol{h}). \tag{A.1}$$

The total anisotropy energy, including (1) uniaxial anisotropy with an easy axis along $\boldsymbol{X}$ and a uniaxial anisotropy energy density parameter K_U and (2) cubic anisotropy with principal axes along $\boldsymbol{X}$, $\boldsymbol{Y}$, and $\boldsymbol{Z}$ and a cubic first order anisotropy parameter K_1, was given in Eq. (1) of Section 2. For convenience, the uniaxial energy term will be denoted as F_U and the cubic energy term as F_1.

The objective of the present analysis is to obtain effective fields, both static and dynamic, in the $\boldsymbol{x}$–$\boldsymbol{y}$–$\boldsymbol{z}$ precession frame introduced in Section 2 through Fig. 2. Recall that in this $\boldsymbol{x}$–$\boldsymbol{y}$–$\boldsymbol{z}$ frame, the static magnetization vector $\boldsymbol{M}_s$ is taken to be co-linear with the x-axis. This means that, to lowest order in the components of $\boldsymbol{M}$, the total magnetization vector in the $\boldsymbol{x}$–$\boldsymbol{y}$–$\boldsymbol{z}$ frame has the defined static M_s component along the x-axis and two dynamic components m_y and m_z along the y- and z-axes, respectively.

There are two basic steps required to obtain the field terms defined through Eqs. (5)–(8) in Section 2. First, one transforms the total energy given in Eqs. (1) and (A.1) as a function of M_X, M_Y, and M_Z into a function of the $\boldsymbol{M}$ components in the x–y–z frame, namely, $M_x = M_s$, $M_y = m_y$, and $M_z = m_z$. Let this transformed energy be specified as $F_{xyz}(M_x, M_y, M_z)$. Second, one evaluates the total effective field in the x–y–z frame as

$$\boldsymbol{H}_{xyz} = -\nabla_M F_{xyz}(M_x, M_y, M_z), \tag{A.2}$$

where ∇_M denotes the gradient operator

$$\nabla_M = \boldsymbol{e}_x \frac{\partial}{\partial M_x} + \boldsymbol{e}_y \frac{\partial}{\partial M_y} + \boldsymbol{e}_z \frac{\partial}{\partial M_z}. \tag{A.3}$$

The static effective field defined through Eq. (6) in Section 2 as H_S is simply the static part of the x-component of $\boldsymbol{H}_{xyz}$, that is, the part which does not contain any M_y or M_z terms. The static parts of the y- and z-components of $\boldsymbol{H}_{xyz}$ must be zero for static equilibrium with $\boldsymbol{M}_s$ along the x-direction. This zero requirement leads to the static equilibrium condition of Eq. (8) in Section 2. The dynamic components of $\boldsymbol{H}_{xyz}$, with the general M_y and M_z factors replaced by the dynamic magnetization components m_y and m_z, lead immediately to the $\boldsymbol{A} \cdot \boldsymbol{m}$ term in Eq. (5) and the $\boldsymbol{A}$ matrix defined in Eq. (7).

The algebra required to obtain the results described above is straightforward. Working expressions for F_H, F_U, and F_1, written in terms of the components of $\boldsymbol{M}$ in the $\boldsymbol{x}$–$\boldsymbol{y}$–$\boldsymbol{z}$ precession frame, are given below:

$$F_H(M_x, M_y, M_z) = -\left\{M_x\left[H_o \cos(\Theta - \Phi) + h_x\right] M_y\left[H_o \sin(\Theta - \Phi) + h_y\right] + M_z h_z\right\}, \tag{A.4}$$

$$F_U(M_x, M_y, M_z) = K_U\left[1 - \frac{M_x^2 \cos^2\Phi + M_y^2 \sin^2\Phi - M_x M_y \sin(2\Phi)}{M_s^2}\right], \tag{A.5}$$

$$F_1(M_x, M_y, M_z) = \frac{K_1}{M_s^4}\left[\tfrac{1}{4}\left(M_x^2 - M_y^2\right)^2 \sin^2(2\Phi) + M_x^2 M_y^2 \cos^2(2\Phi)\right.$$

$$\left. + \tfrac{1}{4} M_x M_y \left(M_x^2 - M_y^2\right) \sin(4\Phi) + \left(M_x^2 + M_y^2\right) M_z^2\right]. \tag{A.6}$$

It should be kept in mind that these terms represent the same free energy as given by Eq. (1), but rewritten in terms of the precessional frame components. It is a straightforward procedure to evaluate the total effective field $\boldsymbol{H}_{xyz}$ from Eqs. (A.2) and (A.3), with $F_{xyz} = F_H + F_U + F_1$.

The total effective field $\boldsymbol{H}_{xyz}$ obtained from Eqs. (A.2), (A.3), (A.4), (A.5) and (A.6) will have several categories of terms. First, there will be terms which contain only M_x factors, with no M_y or M_z factors. Since to lowest order, M_x is equal to the saturation magnetization M_s, these pure M_x terms in $\boldsymbol{H}_{xyz}$ represent the static effective field. As indicated above, the x-component of this static effective field is given by the H_S expression in Eq. (6) of Section 2. Note that this component is parallel to the static magnetization vector $\boldsymbol{M}_s$. The y-component of this static effective field is given by the left-hand side expression in Eq. (8) of Section 2.

For equilibrium with the static magnetization in the x-direction, this y-component field must vanish. This is the origin of the zero condition in Eq. (8).

Turn now to the remaining terms in $\boldsymbol{H}_{xyz}$, those which do contain M_y and/or M_z factors. These terms give rise to the dynamic effective field. Note that M_y and M_z are actually the y- and z-components of the dynamic magnetization $\boldsymbol{m}(\boldsymbol{r},t)$ introduced in Section 2. For this linear, first order theory, the dynamic response is taken to be small. If only first order terms in M_y and M_z are retained, the dynamic effective field part of $\boldsymbol{H}_{xyz}$ reduces to the $\boldsymbol{A}\cdot\boldsymbol{m}$ part of Eq. (5), with the matrix $\boldsymbol{A}$ as given in Eq. (7).

Although not needed for the present analysis, it is useful to keep in mind the demagnetizing self energy for the thin film which enters into the usual uniform mode ferromagnetic resonance (FMR) analysis, $F_D = 2\pi(M_Z)^2$. In the FMR analysis, this term would contribute a stiffness field term of $+4\pi M_s$ to H_α and leads to the FMR frequency position at Ω_B. The '1' term in the definition of Ω_B in Eq. (37) is really a manifestation of this demagnetizing self energy term which is obtained, in the magnetostatic theory, through the boundary value problem.

References

[1] M.J. Hurben and C.E. Patton, J. Magn. Magn. Mater. 139 (1995) 263.
[2] T. Holstein and H. Primakoff, Phys. Rev. 58 (1940) 1098.
[3] J.H.E. Griffiths, Nature 158 (1946) 670.
[4] C. Kittel, Phys. Rev. 73 (1948) 155.
[5] L.R. Walker, Phys. Rev. 105 (1957) 390.
[6] P. Röschmann and H. Dötsch, Phys. Status Solidi (b) 82 (1977) 11.
[7] R.W. Damon and J.R. Eshbach, J. Phys. Chem. Solids 19 (1961) 308.
[8] J.C. Sethares, RADC-TR-83-15, in: Proc. 1981 RADC Microwave Magnetics Technology Workshop, June 10–11, 1981, Rome Air Development Center, Air Force Systems Command (Griffiss Air Force Base, New York, 1983); J.P. Parekh, Circ. Syst. Signal Proc. 4(1/2) (1985).
[9] D.D. Stancil, Theory of Magnetostatic Waves (Springer, New York, 1993).
[10] P. Kaboš and V.S. Stalmachov, Magnetostatic Waves and Their Applications (Chapman and Hall, London, 1994).
[11] G.P. Rodrique, IEEE Trans. Microwave Theory Tech. 11 (1963) 351.
[12] C. Vittoria, J. Magn. Magn. Mater. 21 (1980) 109.
[13] C.E. Patton, IEEE Trans. Magn. 24 (1988) 2024.
[14] See, for example, Proc. First Int. Symp. on Metallic Multilayers, March 1–5, 1993, Kyoto, Japan, S. Maekawa, H. Fujimori, T. Shinjo and R. Yamamoto, eds., J. Magn. Magn. Mater. 126 (1993).
[15] B. Heinrich and J.F. Cochran, Adv. Phys. 42 (1993) 523.
[16] L.R. Bickford, Phys. Rev. 78 (1950) 449.
[17] D.W. Healey, Phys. Rev. 86 (1952) 1009.
[18] J.O. Artman, Phys. Rev. 105 (1957) 74.
[19] C. Vittoria, G.C. Bailey, R.C. Barker and A. Yelon, Phys. Rev. B 7 (1973) 2112.
[20] L. Baselgia, M. Warden, F. Waldner, S.L. Hutton, J.E. Drumheller, Y.Q. He, P.E. Wigen and M. Maryško, Phys. Rev. B 38 (1988) 2237.
[21] I. Bady and E. Schlömann, J. Appl. Phys. 33 (1962) 1377.
[22] E. Schlömann, R.I. Joseph and I. Bady, J. Appl. Phys. 34 (1963) 672.
[23] W. Haubenreiser, D. Linzen and E. Glauche, Phys. Status Solidi 1 (1961) 764.
[24] W. Haubenreiser and D. Linzen, Phys. Status Solidi 2 (1962) 734.
[25] W. Haubenreiser and D. Linzen, Phys. Status Solidi 3 (1963) 133.
[26] W. Haubenreiser, T. Klupsch and F. Voigt, Phys. Status Solidi (b) 66 (1974) 9.
[27] Y.M. Yakovlev and Y.N. Burdin, Sov. Phys. Solid State 16 (1974) 299.
[28] W. Haubenreiser, T. Klupsch and F. Voigt, Phys. Status Solidi (b) 73 (1976) 11.
[29] C.E. Patton and W. Jantz, IEEE Trans. Magn. 14 (1978) 698.
[30] C.E. Patton, Phys. Status Solidi (b) 92 (1979) 211.
[31] C.E. Patton, Phys. Status Solidi (b) 93 (1979) 63.
[32] B. Schneider, Phys. Status Solidi (b) 51 (1972) 325.
[33] B. Schneider, Phys. Status Solidi (b) 66 (1974) 99.

[34] H. Reimann and F. Waldner, IEEE Trans. Magn. 15 (1979) 1720.
[35] R.A. Lemons and B.A. Auld, J. Appl. Phys. 52 (1981) 7360.
[36] G. Rupp, W. Wettling, R.S. Smith and W. Jantz, J. Magn. Magn. Mater. 45 (1984) 404.
[37] O.A. Chilcheva, A.G. Gurevich and L.M. Emiryan, Sov. Phys. Solid State 29 (1987) 61.
[38] R. Gieniusz and L. Smoczynski, J. Magn. Magn. Mater. 66 (1987) 366.
[39] S.P. Li and L.E. Cross, Phys. Status Solidi (b) 159 (1990) 861.
[40] N.S. Almeida and D.L. Mills, Phys. Rev. B 38 (1988) 6698.
[41] M.C. Oliveros, N.S. Almeida, D.R. Tilley, J. Thomas and R.E. Camley, J. Phys. Condensed Matter 4 (1992) 8497.
[42] F.C. Nörtermann, R.L. Stamps, R.E. Camley, B. Hillebrands and G. Güntherodt, Phys. Rev. B 47 (1993) 3225.
[43] M. Sparks, Phys. Rev. B 1 (1970) 3831.
[44] R.E. DeWames and T. Wolfram, J. Appl. Phys. 41 (1970) 987.
[45] T. Wolfram and R.E. DeWames, Phys. Rev. B 4 (1971) 3125.
[46] B.A. Kalinikos, IEE Proc. (London) 127(H1) (1980) 4.
[47] B.A. Kalinikos and A.N. Slavin, J. Phys. C 19 (1986) 7013.
[48] C. Kittel, Phys. Rev. 110 (1958) 1295.
[49] G.T. Rado and J.R. Weertman, J. Phys. Chem. Solids 11 (1959) 315.
[50] C.E. Patton, Phys. Rep. 103 (1984) 251.
[51] B. Hillebrands, Phys. Rev. B 41 (1990) 530.
[52] R.L. Stamps and B. Hillebrands, Phys. Rev. B 43 (1991) 3532.
[53] M.G. Cottam, ed., Linear and Nonlinear Spin Waves in Magnetic Films and Superlattices (World Scientific, Singapore, 1994).
[54] W.H. von Aulock, Handbook of Microwave Ferrite Materials (Academic Press, New York, 1965).
[55] J.F. Cochran, J.M. Rudd, W.B. Muir, G. Trayling and B. Heinrich, J. Appl. Phys. 70 (1991) 6545.
[56] J.R. Truedson, K.D. McKinstry, P. Kabos and C.E. Patton, J. Appl. Phys. 74 (1993) 2705.
[57] B. Lax and K.J. Button, Microwave Ferrites and Ferrimagnetics (McGraw-Hill, New York, 1962) p. 150.
[58] H.J. Van Hook, J.J. Green, F. Euler and E.R. Czerlinsky, J. Appl. Phys. 39 (1968) 730.
[59] C.E. Patton, Phys. Rev. 179 (1969) 352.
[60] R.W. Damon and H. van de Vaart, J. Appl. Phys. 36 (1965) 3453.